# Doctoral Dissertation

**Development of honeycomb-type retinal prosthesis devices integrating a smart CMOS system and chemically-derived iridium oxide electrodes**

**スマート CMOS システムと化学誘導酸化イリジウム電極を融合したハニカム型人工視覚デバイスの開発**

Kuang-Chih Tso

September 2021

Division of Materials Science

Graduate School of Science and Technology

Nara Institute of Science and Technology

# Abstract

High-efficiency neural stimulation plays a role in the development of bioelectronics. An implantable bioelectronic using chemically inert and flexible substrate is introduced to satisfy the requirements in this research. We proposed a honeycomb-type retinal device by integrating a ceramic, parylene encapsulation, and CMOS system via MEMS processes in the application of suprachoroidal-transretinal stimulation (STS). In the proposed device structure, the conjunctional ceramic substrates composed of large stimulating electrodes provide a high-resolution artificial vision. Meanwhile, input wirings could be tremendously reduced by logical and switchable circuits embedded in CMOS microchip that is able to precisely control a stimulating action of electrodes to obtain an artificial vision for visual disease remedies. The CMOS system brings the MEMS process applicable for developing the dedicated device. A chemical bath deposition of iridium oxide was used for electrode fabrication to serve as the high-performance stimulating electrodes. The morphology, chemical-state, electrochemical properties of the electrodes are investigated in this research by SEM, XPS, and potentiostat/galvanostat, respectively. The result shows that a chemical bath deposition of the iridium oxide is the applicable process to fabricate the stimulating electrodes, and its electrochemical performances are higher than sputtered iridium oxide electrodes. With the facile fabrication of electrodes and device, the proposed retinal device adopting CBD-derived

iridium oxide electrodes is able to provide a promising implantable device for suprachoroidal-transretinal stimulations.

# Acknowledgement

This research was carried out under the warm guidance of Prof. Jun Ohta, Photonic Device Science Laboratory, Graduate School of Science and Technology, Nara Institute of Science and Technology. Prof. Jun Ohta kindly provided guidance based on his specialized knowledge, from his research policy to consideration of experimental results. In addition, I had many opportunities to make presentations at academic conferences, and I was able to lead a fulfilling research life. I would like to express my gratitude and thank you very much.

Prof. Yoichiroh Hosokawa, Department of Materials Science and Technology, Graduate School of Science and Technology, Nara Institute of Science and Technology, provided kind guidance and suggestions to this research and thesis direction. I would like to express my deepest gratitude here.

Prof. Takuya Nakashima, Department of Materials Science and Technology, Graduate School of Science and Technology, Nara Institute of Science and Technology, provided useful guidance and suggestions to this research and thesis direction. I would like to express my deepest gratitude here.

Prof. Kiyotaka Sasagawa, Department of Materials Science and Technology, Graduate School of Science and Technology, Nara Institute of Science and Technology, provided useful guidance and suggestions to this research and thesis direction. I would like to express my deepest gratitude here.

Prof. Makito Haruta, Department of Materials Science and Technology, Graduate School of Science and Technology, Nara Institute of Science and Technology, provided the in carrying out this research. I also received useful guidance and suggestions based on our abundant knowledge of experiments using the MEMS process and device designs. He is not only my academic advisor but also the Japanese advisor. He treats me like a closed friend, taking me to experience the true and local Japan life. Without his accompany, I think I cannot finish my study in NAIST. I would like to express my deepest gratitude here.

Prof. Hiroyuki Tashiro provided valuable guidance and suggestions about the bio-knowledges, electrochemical knowledges, and surgery operation skills. He is always being kind to teach me the research and arrange the animal experiment for us. I would like to express my deepest gratitude here.

Prof. Hironari Takehara provided useful guidance and suggestions based on his abundant knowledge about sputtering and photolithography process. I would like to express my deepest gratitude here.

I would like to thank Prof. Toshihiko Noda for kindly being my first contact person to this study in Japan. He is always being kind and willing to teach me the knowledge he has, without his warm and valuable guildances, I cannot finished the double degree in NAIST. I would like to express my deepest gratitude here.

I would like to thank Prof. Pu-Wei Wu, Department of Materials Science, National Yang Ming Chiao Tung University (Taiwan), for his kind guidance and encourages me to study for the double degree with NASIT. I would like to express my deepest gratitude here.

Dr. Jyh-Fu Lee, National Synchrotron Radiation Research Center (Taiwan), for his warm guidance and science knowledge especially in XAS technique. Without his advice, I cannot learn the XAS well by myself. I would like to express my deepest gratitude here.

I would like to thank Prof. Emeritus Chung-Yu (Peter) Wu for kindly supporting about the strong collaboration between the NAIST and NYCU. Without his organization and such an excellent research, I cannot finish my double degree in NASIT. I would like to express my deepest gratitude here.

I would like to thank Prof. Yu-Ting Cheng for kindly being my committee member of the double degree in NAIST and NYCU. I received guidances about my research in NAIST from his valuable suggestions. I would like to express my deepest gratitude here.

Prof. Po-Chun Chen, Department of Materials and Mineral Resources Engineering, National Taipei University of Technology, for his kind guidance and encourages me to study the double degree with NAIST. I would like to express my deepest gratitude here.

For all of our collaborative research partners, including NIDEK Co., Ltd. Artificial Vision Research Institute, Director Yasuo Terasawa, Dr. Yukari Nakano, and Mr. Takuro Takano, we will provide ceramic substrates, sputtering, CMOS chip processing, and more. We received generous support such as animal experiments. I would like to express my deepest gratitude here.

The laboratory

Postdoctoral fellow

Dr. Yasumi Ohta, Dr. Erus Rustami

Researcher

Mamiko Kawahara, Akihiro Kanda, Noriaki Matsuura, Shigeo Okuto, Akari Hotta

Contract researcher

Mr. Kenzo Kanedo, Mr. Akihiko Futada

Received a great deal of help, such as management of experimental equipment, guidance on handling, and experimental assistance. I would like to express my deepest gratitude here.

I would like to thank Dr. Yasumi Ohta for kindly supporting my mental life in Japan, she takes careful of me and oftenly makes a warm and sweet dissert to me and everyone in the lab. I really appreciate it. I also received the guidances in NAIST from her valuable suggestions. I would like to express my deepest gratitude here.

The laboratory and secretary, Ms. Ryoko Fukuzawa, provided encouraging support in the administrative procedures and application documents associated with the research activities. She always helps me out in many things especially I made mistakes on some documents. I would like to express my deepest gratitude here.

Mr. Hiroki Endo, a graduate of the master's program at the same laboratory, provided a lot of guidance and advice on artificial vision, including the succession of this research. I would like to express my deepest gratitude here.

I would like to specially thank Mr. Yuki Fukunari, OB student, and Miss. Mizuki Hagita, 2$^{nd}$ year master student, for their cooperation in taking over this research, such as assisting experiments, exchanging opinions, and organizing experimental data. I would like to express my deepest gratitude here.

2nd year doctoral course

Mr. Yasuto Mori, Mr. Ze Wang, Mr. Rebusi Romeo Brioso,

Mark Christian Guinto, Pakpuwadon Thanet,

Teixeira Sais Barbara, Mohamad Izzat Asmer Bin Adnan, Kyosuke Naganuma

1st year doctoral course

Natcha Kulmala, Joshua Olorocsimo Philippe, Kenji Sugie,

Nicha Sato, Honghao Tang, Latiful Akbar

2st year master's program

Ryoma Okada, Noriaki Kishida, Kazuaki Kurasawa,

Ryota Shioya, Takaaki Murakami

Received a lot of knowledge and inspiration during daily discussions. Also, during my student life, I was indebted to both public and private. We would like to express our deepest gratitude here.

In addition, we received advice and guidance from many people, including seniors who have graduated from the same laboratory. We would like to express our deepest gratitude here.

The animal experiments in this study were conducted in accordance with the animal experiment regulations of NIDEK Co., Ltd. We pray for the souls of the animals that were sacrificed due to the progress of this science and technology.

Finally, I would like to express my deep gratitude to my family for supporting my student life, personal life. Their supports are very important to nurture my mind and my health.

Importantly, Miss Shih-Ting Lan, my love, always supports and stays with me even we lived in different places (Japan and Taiwan) that makes me being love and home. Without your 100% supports to my decision to study this double degree, I cannot be who I am now. Thank you so much for your sweet and warm supports.

# Content

**Abstract**.....1

**Acknowledgement**.....3

**1. Introduction**.....13

1.1 Background.....13

1.2 Purpose of this research.....14

**2. Retinal prosthesis devices**.....16

2.1 Overview of the retinal prosthesis devices.....16

2.2 Concept of the retinal prosthesis devices.....17

2.2.1 Epi-retinal prosthesis device.....18

2.2.2 Sub-retinal prosthesis device.....20

2.2.3 Suprachoroidal trans-retinal prosthesis device.....21

2.3 Stimulation electrodes.....23

2.3.1 Material candidates.....23

2.3.2 Syntheses of iridium oxide electrodes.....25

**3. Experimental**.....29

3.1 Fabrication of the honeycomb-type retinal prosthesis devices.....29

3.1.1 Design of the retinal device.....29

3.1.2 The ceramic substrate.....30

3.1.3 The CMOS system.....31

3.1.4 Platinum interconnections.....34

3.1.5 Stimulating electrodes.....35

3.1.5.1 Chemical bath deposition of iridium oxide thin film.....36

3.1.5.2 Sputtering deposition of iridium oxide electrodes.....43

3.1.6 Assembly of the retinal device.....50

**4. Results and discussion** ..... 62

4.1 Characterization of the stimulating electrodes ..... 62

4.2 Electrochemical evaluation of the stimulating electrodes ..... 64

4.2.1 Cyclic voltammetry (CV) ..... 65

4.2.2 Voltage transient ..... 67

4.2.3 Electrochemical impedance spectroscopy (EIS) ..... 69

4.3 Comparison the CBD and sputtering processes of iridium oxide electrodes ..... 70

4.4 Evaluation of the retinal device ..... 74

4.4.1 Operation system and setup ..... 74

4.5 *In vitro* experiment ..... 77

4.6 *In vivo* experiment ..... 79

4.6.1 *In vivo* experimental system ..... 80

4.6.2 *In vivo* measurement results ..... 82

4.6.3 Summary of the *in vivo* experiment ..... 83

**5. Conclusion** ..... 85

5.1 Summary ..... 85

5.2 Future outlook ..... 86

**References** ..... 88

**List of Publications** ..... 91

# List of figures

**Figure 1.1** The projections for the AMD patient in 2030 to 2050

**Figure 1.2** The schematic diagram of the thesis structure

**Figure 2.1** The types of the retina prosthesis devices

**Figure 2.2** The conceptual diagram for the retina prosthesis devices

**Figure 2.3** The schematic diagram for the Argus-II

**Figure 2.4** The schematic diagram for the Alpha AMS system

**Figure 2.5** The schematic diagram for the STS system fabricated by NIDEK

**Figure 2.6** The schematic diagram of the sputtering deposition of the iridium oxide film

**Figure 3.1** The schematic of the retina device

**Figure 3.2** The structure of the ceramic substrate a) front view, b) rear view, and c) tilt view

**Figure 3.3** The layout of the ceramic substrate

**Figure 3.4** The specification and block diagram of the CMOS chip

**Figure 3.5** The interconnects layout in 1 and 7 modules

**Figure 3.6** The sample preparation for the photolithography process

**Figure 3.7** The photographs of the CBD-derived iridium oxide thin film on a ceramic substrate by using a photoresist pattern

**Figure 3.8** The photographs for a ceramic substrate of (a) parylene coating, (b) parylene ablation on electrodes, and (c) chemical bath deposition of iridium oxide thin film on the platinum electrodes

**Figure 3.9** The fabrications of iridium oxide electrodes in (a) CBD process, (b) the chemical bath preparation

**Figure 3.10** The structure of the iridium oxide thin film sample

**Figure 3.11** The CV measurement setup for optimizing sputtered iridium oxide thin film

**Figure 3.12** The CV measurement setup for optimizing sputtered iridium oxide thin film

**Figure 3.13** The flowchart for sputtering iridium oxide electrodes

**Figure 3.14** The flowchart of retinal device fabrication

**Figure 3.15** The detailed flowchart for platinum interconnects patterning

**Figure 3.16** The photographs of the patterned photoresist (left), and the final platinum interconnects (right)

**Figure 3.17** The schematic diagram for flip-chip bonding position

**Figure 3.18** The schematic diagram for sacrificial layer coating and detachment

**Figure 3.19** The schematic diagram for sacrificial layer coating and detachment

**Figure 3.20** The photographs for the final retinal prosthesis device

**Figure 4.1.** The SEM images of CBD-iridium oxide electrode array

**Figure 4.2** The XPS profile for CBD and sputtered iridium oxide electrode. (a) Ir 4f spectra and O 1s profile of (b) CBD-derived, and (c) sputtered iridium oxide thin film

**Figure 4.3** The graphic flowchart for wiring process

**Figure 4.4** The setup for electrochemical measurements

**Figure 4.5** The cyclic voltammetry profile for the CBD-iridium oxide electrodes compared to the sputtered iridium oxide

**Figure 4.6** The voltage transient profile for CBD-derived and sputtered iridium oxide electrode

**Figure 4.7** The impedance responses for CBD-derived and sputtered iridium oxide electrode

**Figure 4.8** The electrochemical durability for CBD-derived iridium oxide electrode

**Figure 4.9** The schematic of a) the operation system of the device, b) the experimental setup of the device operation

**Figure 4.10** The stimulation program interface

**Figure 4.11** The definition of the stimulation waveform and electrode IDs

**Figure 4.12** The current response for the device performance in various input biphasic currents

**Figure 4.13** The comparison of devices fabricated from the previous and new process in current response profile (800 μA)

**Figure 4.14** The system for the *in vivo* experiment

**Figure 4.15** The *in vivo* experiment photographs of (a) device implantation, (b) cross sectional view of the rabbit eye, and (c) optical coherence tomography

**Figure 4.16** The stimulation waveform in the *in vivo* experiment

**Figure 4.17** Device after *in vivo* experiment

**Figure 4.18** The in vitro experiment after *in vivo* experiment

# List of tables

**Table 2.1** The summary of stimulation electrodes

**Table 3.1** The formula for chemical bath deposition of iridium oxide

**Table 3.2** The parameter of photolithography process

**Table 3.3** The parameter of the parylene patterning on ceramic substrate for CBD-iridium oxide film

**Table 3.4** The sputteting parameter for iridium oxide electrodes

**Table 3.5** The deposition condition of the parylene layer for device assembly process

**Table 3.6** The sputteting parameter for platinum interconnects

**Table 3.7** The preparasion condition for silane coupling solution

**Table 3.8** The condition for gold bump formation

# 1. Introduction

## 1.1 Background

Recently, the number of patients suffering from retinal neuron degeneration, such as retinitis pigmentosa (RP) and age-related macular degeneration (AMD) has significantly increased as shown in Figure 1.1 [1, 2]. These visual diseases are generally difficult to be diagnosed and treated. Thus, researchers have been devoted to remedying visual diseases by integrating electronics and neuron engineering. For decades, implantable bioelectronics has been widely developed to replace degenerated neurons with functional bioelectronics [3-14]. The underlying therapeutic principle of implantable bioelectronics is to apply electrical charge across bio-electrodes to stimulate the neurons and initiate a neural action potential (AP) so that the stimulated neuron can propagate the manipulated electrical signals from bioelectronics to the neuron network to achieve neural recovery.

The critical part of retinal neuron stimulation is the interface with retinal neurons. Thus, the stimulating electrode must be biocompatible and must have a distinct electrochemical performance. According to the specifications mentioned above, the common stimulating electrode materials are platinum, platinum-iridium, titanium nitride, and iridium oxide [15-18]. Among these electrode materials, the iridium oxide shows higher charge storage and delivery capacity than platinum-based or TiN electrodes owing to the additional faradaic reaction in which the charge can be stored and delivered in the case of the iridium oxide electrode.

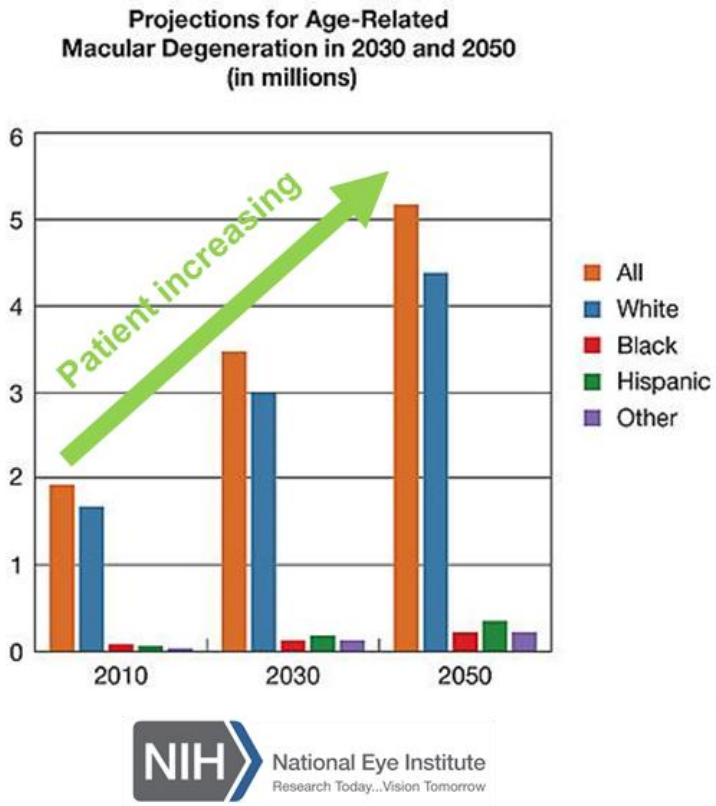


**Figure 1.1** The projections for the AMD patient in 2030 to 2050 [19]

## 1.2 Purpose of this research

In this research, we propose a honeycomb-type STS device that consists of a robust and flexible structure that aims to improve neuron function. Initially, we established a fabrication process to assemble the device in a smart CMOS platinum-based electrodes system. After the fabrication for the smart CMOS electrodes system was completed, a neuron interface was developed by using high-performance material which is iridium oxide. In the synthesis of iridium oxide electrodes, we investigated a sputtering process and a unique solution-based process to fabricate iridium oxide electrodes to serve as high-performance stimulating electrodes. The electrochemical properties of the final iridium oxide electrodes prepared from

different syntheses are discussed. Finally, we concluded the final synthesis to fabricate the iridium oxide electrodes that are to be introduced in the smart CMOS electrodes system.

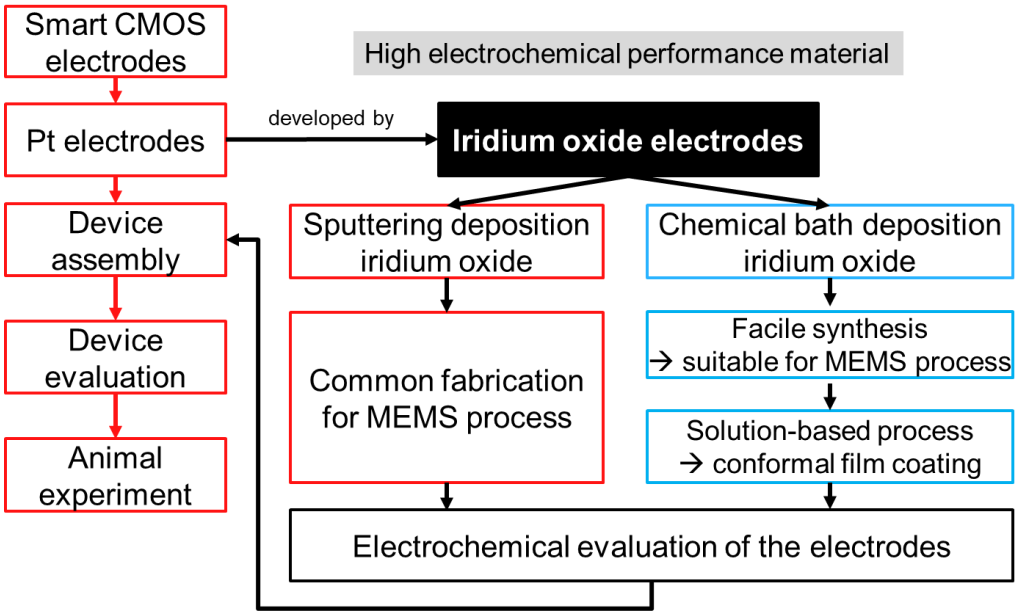


Figure 1.2 The schematic diagram of the thesis structure

# 2. Retinal prosthesis devices

## 2.1 Overview of the retinal prosthesis devices

To date, retinal implants have been developed for commercial use, such as Argus-II (Second Sight Inc., USA), Alpha IMS (Retina Implant AG, Germany), and DPSS (A-neuron, Taiwan) [9, 10, 19-21]. The retinal prostheses could be implanted in different locations of the retina as shown in Figure 2.1. The Argus-II and Alpha IMS are implanted in the epi-retina and sub-retina, respectively. These retinal prostheses implants are highly invasive, and carry high risk. Among the various visual implants, the suprachoroidal-transretinal stimulation (STS) implant is considered as a much safer stimulation approach, as per clinical trials. For example, Bionic Vision Australia (BVA, Australia) and Japan's Artificial Vision Project (NIDEK, Japan) have successfully demonstrated the practical retinal implant through the STS approach [22-24]. In previous studies, we have reported the STS device with platinum and sputtered iridium oxide as the stimulated electrodes [3-5].

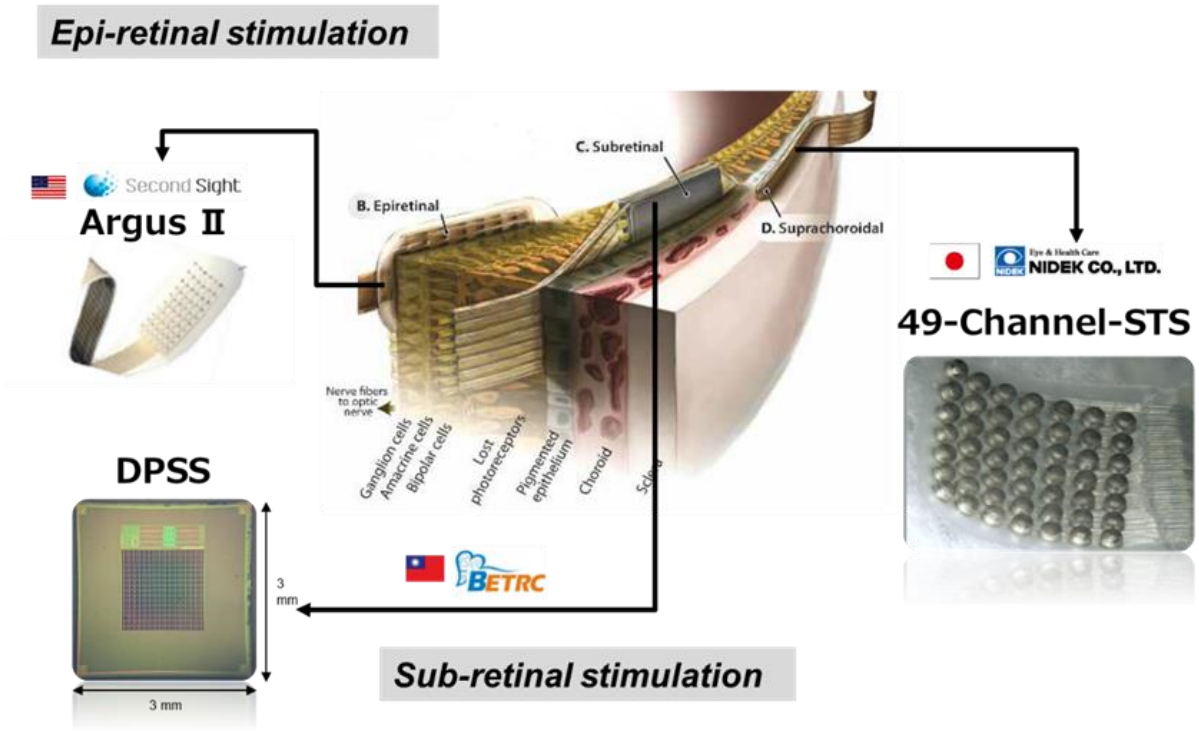


**Figure 2.1** The types of the retina prosthesis devices [6]

## 2.2 Concept of the retinal prosthesis devices

As mentioned in 2.1, an artificial vision system has been widely developed in the world. Figure 2.2 shows the configuration of the artificial vision system. The artificial vision system consists of an external device and an internal device connected by wireless communication. Visual information is acquired via an extra camera, which is an extracorporeal device. The acquired visual information is transmitted from the primary coil outside the body to the secondary coil inside the body together with electric power. Then, the stimulation pattern is demodulated by the stimulation circuit which is based on the transmitted visual information, and electrical stimulations are performed on the retina neurons. The neurons would be evoked (so-called neuron firing) by electrical stimulations, at this moment, the evoked neurons would

start propagating the signal through a series of a complicated neural network to the visual cortex of the brain via the optic nerve, causing an artificial light sensation which is called phosphene.

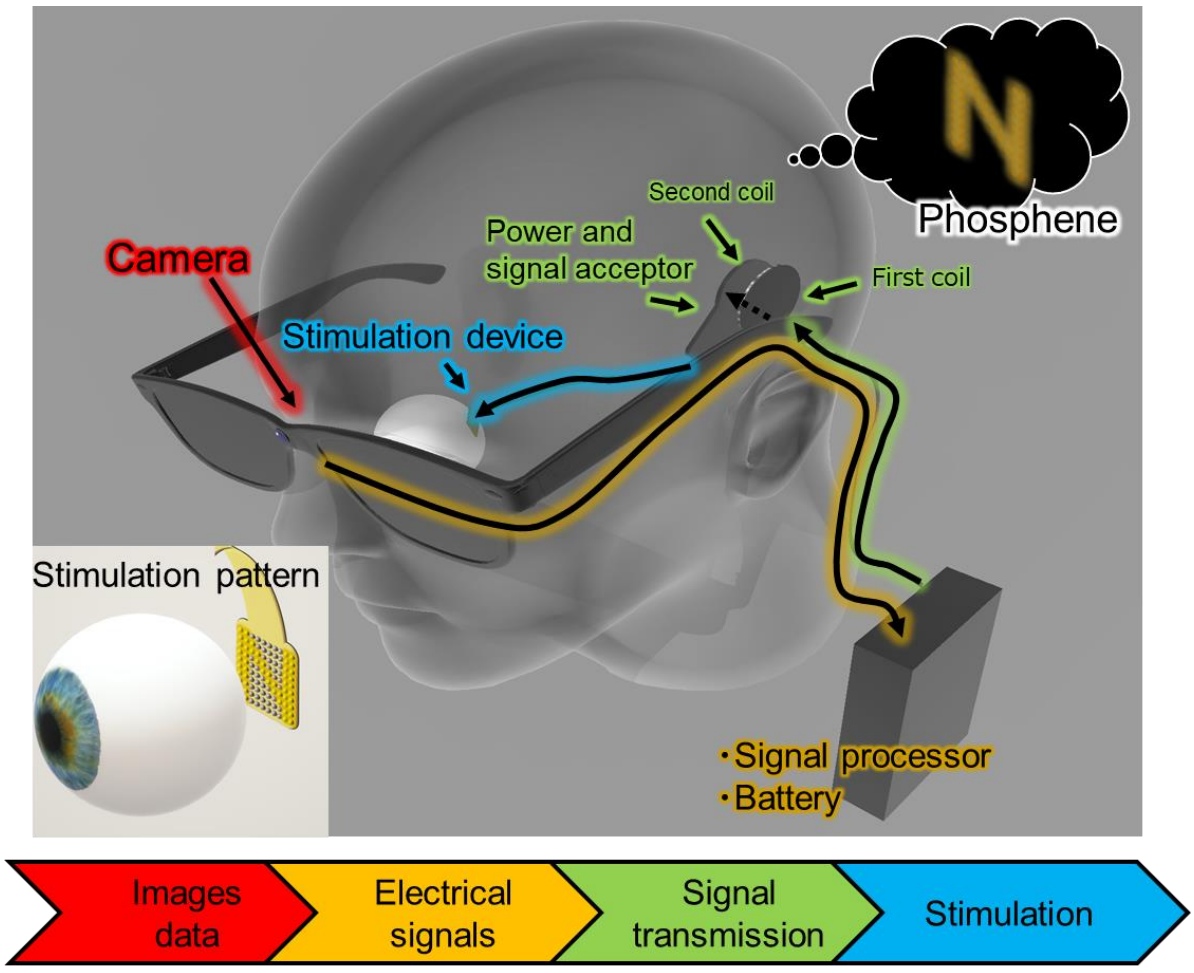


**Figure 2.2** The conceptual diagram for the retina prosthesis devices

### 2.2.1 Epi-retinal prosthesis device

The epi-retinal stimulation is a method of fixing the device to the innermost part of the retina. In this approach, the stimulation threshold to evoke the retinal neurons is low, because the distance between the stimulation electrode and the retina is short, which directly stimulates the ganglion cell that is the final terminal to transmit the signal to the cortex of the brain.

However, the device is required to fix at the epi-retinal layer by tacks or anchors resulting in more invasive and harder to remain the implantation place to the curvature of the eyeball.

Argus I & II of Second Sight Medical Products (SSMP) in the United States is the main research group for epi-retinal stimulation methods. Argus I has shown its usefulness after the long-term implantation of a device equipped with 4 × 4 electrodes for 10 years [25]. Later, Argus II was developed to increase the resolution over Argus I. The Argus II device is shown in Figure 2.6 [26]. Argus II is a retinal device adopting 60 stimulation electrodes. The Argus retinal device is the first product to get the approval of the artificial vision system by the FDA (Food and Drug Administration).

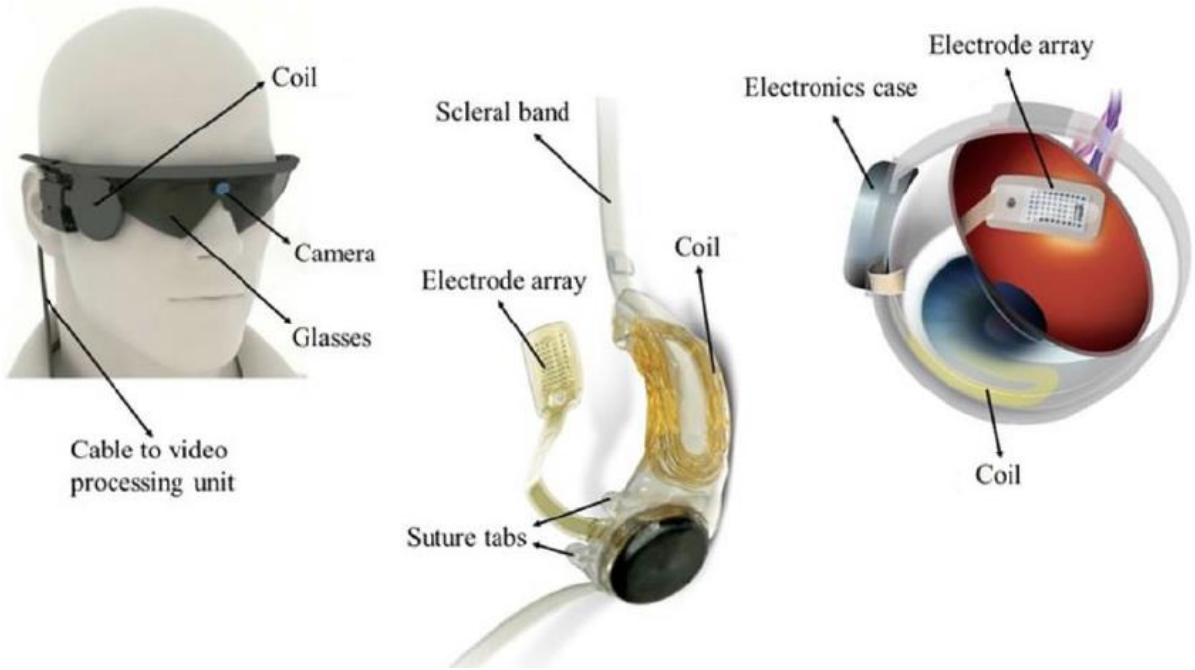


**Figure 2.3** The schematic diagram for the Argus-II [7]

### 2.2.2 Sub-retinal prosthesis device

Sub-retinal stimulation is an approach in which a device is implanted between the retina and the choroid. This approach does not require the tacks unlike the epi-retinal stimulation method, because the sub-retinal device is fixed by intraocular pressure of the retina.

In the sub-retinal stimulation approach, the electrode and the light receive visual information on the same side so that the visual information is received in conjunction with the movement of the eyeball to reconstruct the visual information which is close to the original behavior to see visions. However, due to the implantation position, the device can block the transport of nutrients in which a space between the retina and the choroid. Therefore, there is a concern that retinal tissue may be further caused atrophy during long-term implantation [27]. Two approaches have been investigated for the sub-retinal stimulation approach. There are (a) an approach using a standard electrode array and (b) an approach using a Micro-Photodiode-Array (MPDA). The method using a standard electrode array acquires images from an extra camera and conducts electrical stimulation by the electrode array, but MPDA does not require the extra camera because MPDA has the photodiode to detect the incident light.

The main research group for sub-retinal stimulation is Retina Implant. Devices developed by Retina Implant include Alpha-IMS and Alpha-AMS. Alpha-IMS uses MPDA to detect light and then to generate stimulating currents, and an external power supply circuit is provided to amplify the photocurrent. This device is adopted with 1,500 stimulating electrodes, and the

electrode material is titanium nitride. The device is already in clinical trials. Figure 2.4 shows the Alpha-AMS. Alpha-AMS is an improved version of alpha-IMS and it has been reported to have an improved lifespan in clinical trials [28].

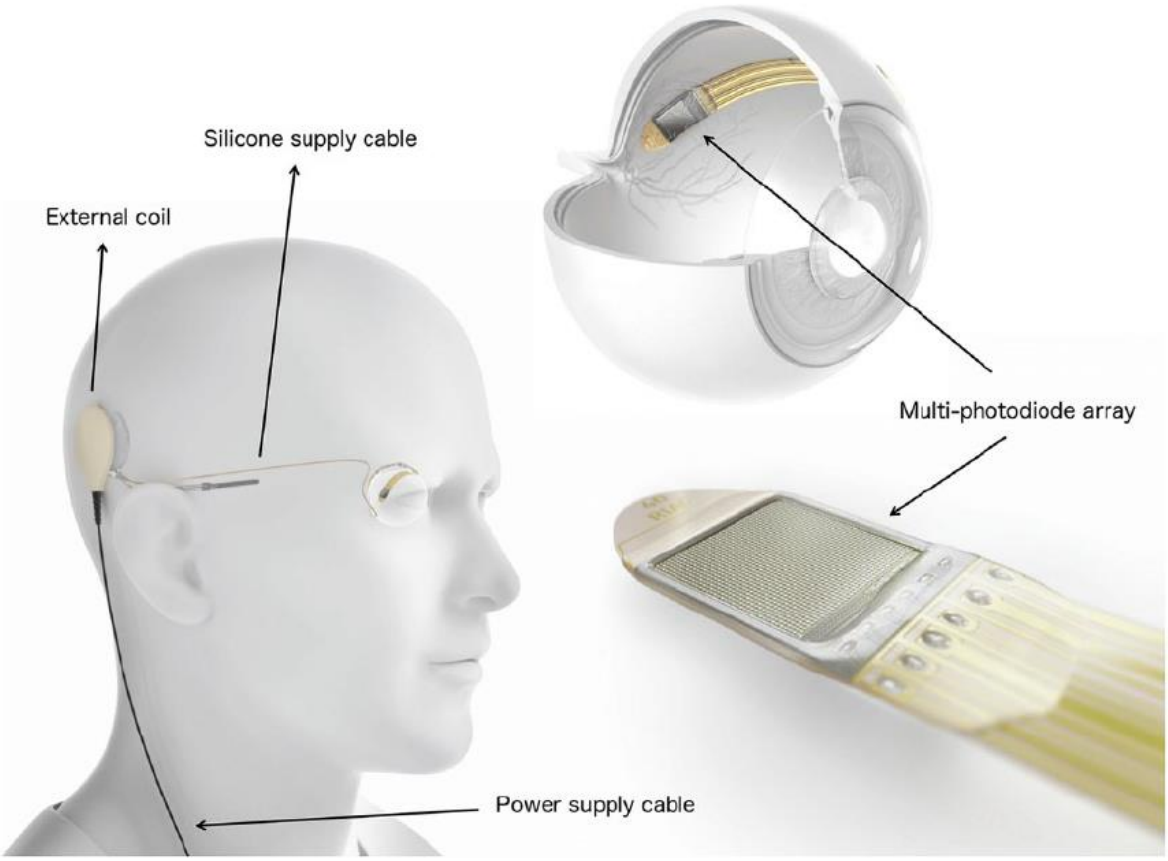


**Figure 2.4** The schematic diagram for the Alpha AMS system [8]

### 2.2.3 Suprachoroidal trans-retinal prosthesis device

The suprachoroidal transretinal stimulation (STS) is an approach where a device is implanted between a choroid and a sclera or in the sclera. Since it is implanted in the sclera far from the retina, the risk of retinal damage during surgery is lower than other approaches, and it

is also the less invasive implantation. On the other hand, since there is a distance to the retina, the applied current or charges hardly affect the neurons resulting in the stimulation threshold becoming higher than other approaches. Therefore, a large stimulation current is required as compared with other approaches. Related research and development are ongoing by NIDEK, a Japanese ophthalmic device manufacturer, a group at Osaka University, and Bionic Vision Australia (BVA) in Australia as the main research groups that use the STS approach. Figure 2.5 shows the STS-type device developed by NIDEK [29]. This device is equipped with 49 stimulating electrodes, and clinical trials have been conducted to confirm its safety during surgery and the induction of phosphene. Clinical studies are being conducted on devices developed by BVA [23].

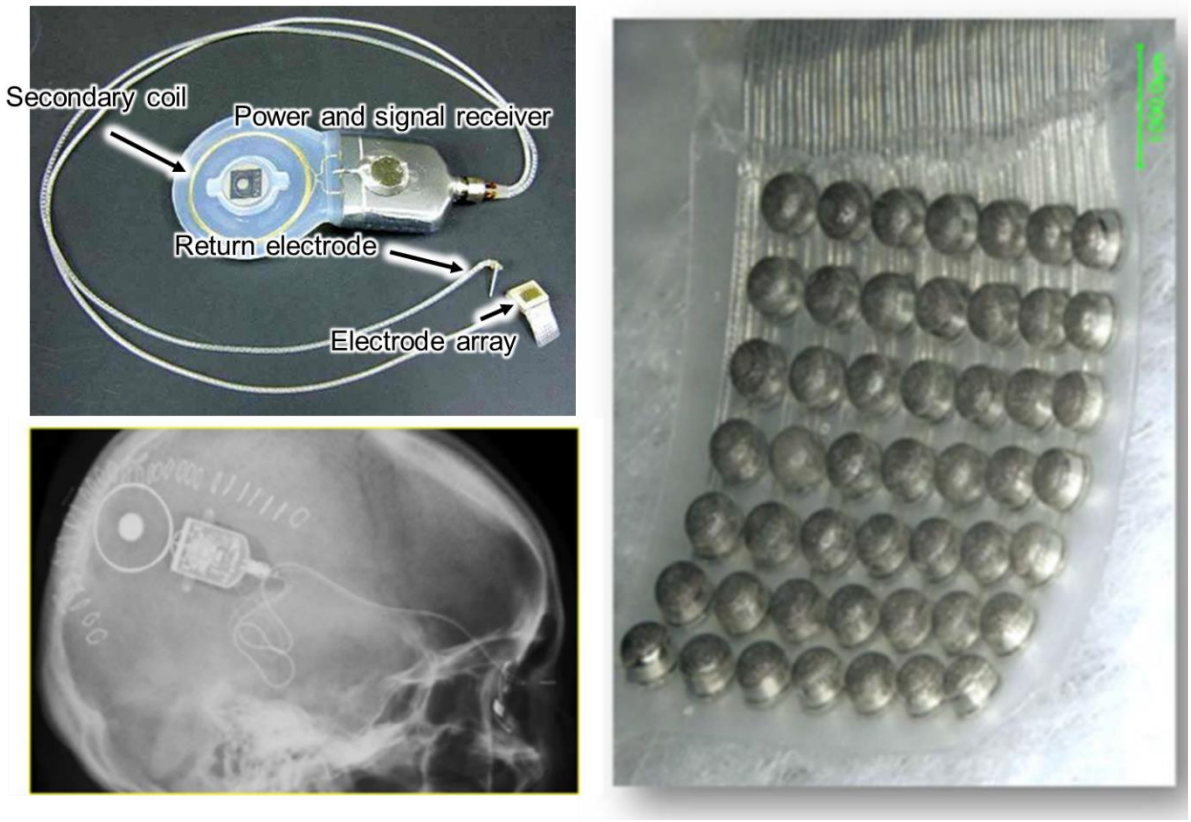


**Figure 2.5** The schematic diagram for the STS system fabricated by NIDEK

## 2.3 Stimulation electrodes

### 2.3.1 Material candidates

For implantable neuron stimulation, the electrode materials must be chemically inert and be capable of providing a high electrical charge to evoke the retinal neurons. To date, platinum, titanium nitride (TiN), and iridium oxide have been considered candidates for stimulation electrodes [30]. The popular material for neuron stimulations is still platinum electrodes due to the chemical state and high tolerance against corrosion [31]. The TiN electrodes have already been used in the Alpha AMS retinal device as mentioned earlier.

However, the literature reported that Pt and TiN electrodes have poor electrochemical properties than iridium oxide electrodes, such as impedance and charge storage/delivery capacity [15-18]. These distinct electrochemical properties in the iridium oxide electrode suggest that the iridium oxide could be a promising stimulation electrode. Accordingly, the charge delivery capacity for Pt, $Ta_2O_5$, and TiN was reported as ~0.15, ~0.5 and ~1 mC/cm$^2$, respectively, which is less than that of the iridium oxide electrode (~5 mC/cm$^2$) [15, 30]. The summary of stimulation electrodes for their electrochemical properties is listed in Table 2.1. Therefore, in this research, we are devoted to developing the stimulation electrode by using iridium oxide.

**Table 2.1** The summary of stimulation electrodes

| Electrode materials | Charge delivery capacity (mC/cm$^2$) | Water window versus Ag\|AgCl (V) |
|---|---|---|
| Pt and PtIr | 0.05 to 0.15 | -0.6 to 0.8 |
| Tantalum oxide ($Ta_2O_5$) | ~0.5 | -0.9 to 0.9 |
| Titanium nitride (TiN) | ~1 | |
| Sputtered iridium oxide | 1 to 5 | -0.6 to 0.8 |
| Thermal iridium oxide | ~1 | |
| Activated iridium oxide | 1 to 5 | |

### 2.3.2 Syntheses of iridium oxide electrodes

#### 2.3.2.1 Sputtering deposition

A sputtering deposition is the most common process to fabricate iridium oxide films. The power source could be divided into two methods, a radio frequency (RF) magnetron sputtering [31, 32] and a direct current (DC) sputtering [16, 33]. The reactive sputtering has become more popular recently, which is due to a DC electric field toward a cathode (a target made from the coating material) accelerates argon ions so that the ionization of the target can be enhanced by applying a magnetic field (magnetron sputtering). It is possible to deposit a combination of elements or compounds such as iridium oxide films by purging adequate reactive gases. However, a high vacuum for deposition conditions and unnecessary target wastes are typical drawbacks of the sputtering process. In addition, the stoichiometry of the iridium oxide film controlled by the sputtering condition is another issue to get a proper deposition of the iridium oxide films. The schematic diagram of the sputtering deposition of the iridium oxide film is shown in Figure 2.6.

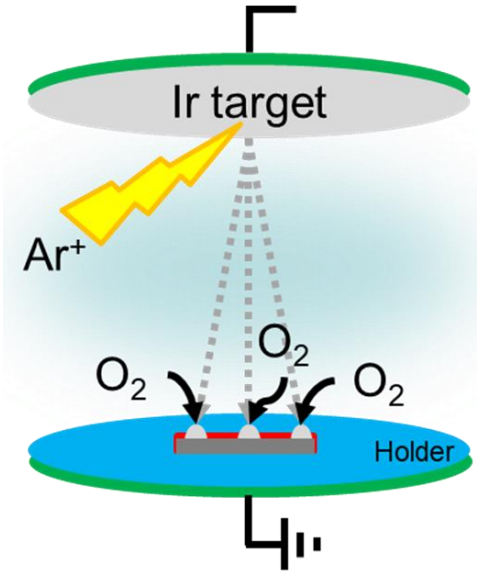


**Figure 2.6** The schematic diagram of the sputtering deposition of the iridium oxide film

2.3.2.2 Thermal decomposition

$IrO_2$ films could also be prepared by thermal decomposition of iridium precursor solution on a chemical-inert substrate such as titanium or tantalum [34]. In literature, the $IrO_2$ film was fabricated on a silicon substrate by thermal decomposition of $H_2IrCl_6$ aqueous solution in the air at 500°C reported by Fierro et al. [35]. Moreover, Kawar et al. deposited iridium oxide films by spraying trihydrated iridium chloride solution on preheated glass substrates from 250 to 400°C [36]. In addition, the as-deposited samples from the decomposition method are transformed into $IrO_2$ films after annealing at 600°C [36, 37]. In general, thermal decomposition involves many parameters, such as distance from the nozzle to substrate, nozzle frequency, solution concentration and spray rate to get a conformal $IrO_2$ film.

#### 2.3.2.3 Electrodeposition

Electrodeposition is one of the popular solution-based processes. It required an external potential or current that applied to the conductive substrate to deposit desirable materials. Three-electrode and two-electrode modes are the common experimental setup for electrodeposition. Electrodeposition can be conducted in potentiostatic mode [38], galvanostatic mode [39], cyclic voltammetry [40], and pulse deposition [41]. In literature, the potentiostatic method, cyclic voltammetry, and pulse deposition have been developed to deposit $IrO_2$ film [38, 40, 41]. The electrodeposition has several advantages such as rapid deposition rate; however, a critical drawback of electrodeposition is that a conductive substrate is required in the electrodeposition. In addition, the deposition electrolyte is required to add suitable complexing agents to stabilize the Ir precursors ($Ir^{3+}$ or $Ir^{4+}$) for preventing undesirable precipitations.

#### 2.3.2.4 Chemical bath deposition

Chemical bath deposition (CBD) is also a solution-based process where the deposited film is formed from the redox reaction taking place in a chemical bath. The chemical bath deposition does not require applying the external potential or current to deposit the film such as metal and metal oxide film [42]. The chemical bath deposition only requires an autocatalytic surface and reducing or oxidizing agents. In addition, complexing agents also could be used to control a deposition rate and deposition lifetime in the chemical bath deposition. This research mainly

introduced the chemical bath deposition to fabricate the iridium oxide thin film to serve as the stimulation electrodes.

# 3. Experimental

## 3.1 Fabrication of the honeycomb-type retinal prosthesis devices

### 3.1.1 Design of the retinal device

The proposed device had a ceramic and flexible parylene structure for STS. Ceramic substrates were used because of their chemical inertness, durability, and widespread applications in medical treatment, resulting in a promising device structure for long-term implantation. The parylene-based retinal device is composed of ceramic substrates with iridium oxide microelectrodes, platinum interconnects, and CMOS (Complementary Metal Oxide Semiconductor) chips. Each ceramic unit was connected by platinum interconnects embedded in parylene, which provided a large stimulating electrode number to achieve the high-resolution artificial vision, as shown in Figure 3.1. The ceramic substrate and the arrangement of electrodes were designed to have a honeycomb shape and hexagonal distribution. This design was to minimize the size of the implantable device with high electrode density, which in turn makes the implantation minimally invasive. The iridium oxide microelectrodes in a hexagonal arrangement allow the patient to potentially obtain high acuity due to the dense spatial distribution of electrodes.

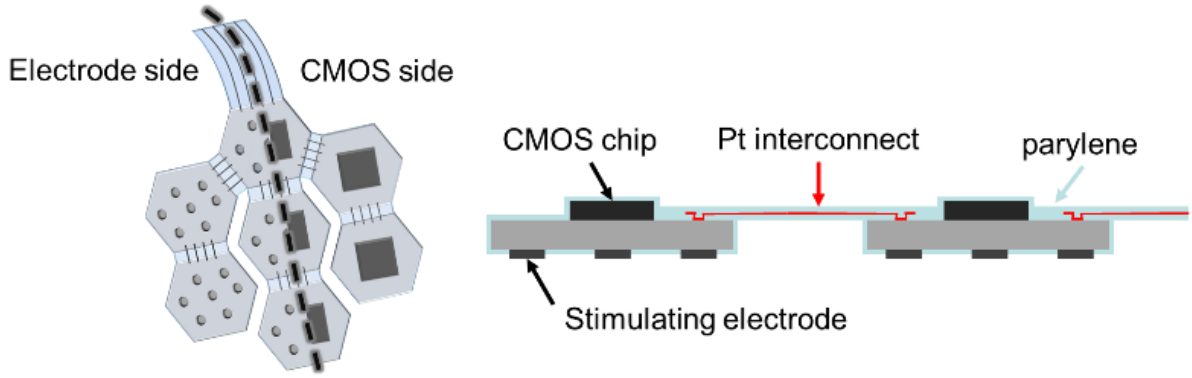


**Figure 3.1** The schematic of the retina device

### 3.1.2 The ceramic substrate

The ceramic was fabricated by Nikko Ceramics Inc., Japan. The shape of the ceramic substrate was hexagonal, and had dimensions of 2.30 mm by 2.65 mm and a thickness of 0.3 mm with the seven platinum electrodes and corresponding platinum pads (VDD, GND, CONT1 and CONT2) as shown in Figure 3.2. In Figure 3.2 (b), the CMOS chip was installed in the white frame area to respectively connect to the pad of VDD, GND, CONT1, CONT2 and 7 electrodes. The pads and internal interconnects are composed of platinum due to the biocompatible concerns instead of copper or nickel. The detailed internal interconnects embedded in the ceramic are displayed in Figure 3.3. At this stage, the stimulating electrodes are made of platinum. To improve the performance of neuron stimulations, we selected iridium oxide as the final stimulating electrode material. Hence, the iridium oxide thin film was further deposited on top of the platinum substrates to serve as the final interface to the neurons. The fabrication of the iridium oxide is discussed later in the experimental sections 3.1.6.

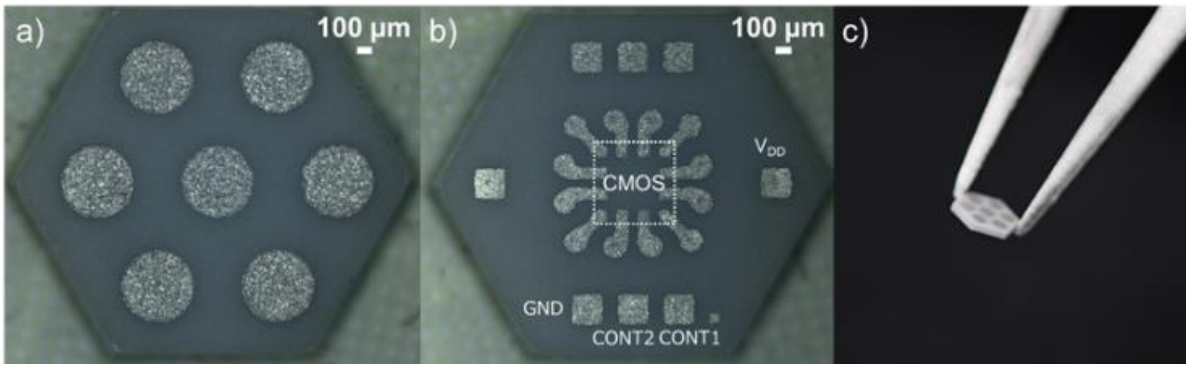


**Figure 3.2** The structure of the ceramic substrate a) front view, b) rear view, and c) tilt view.

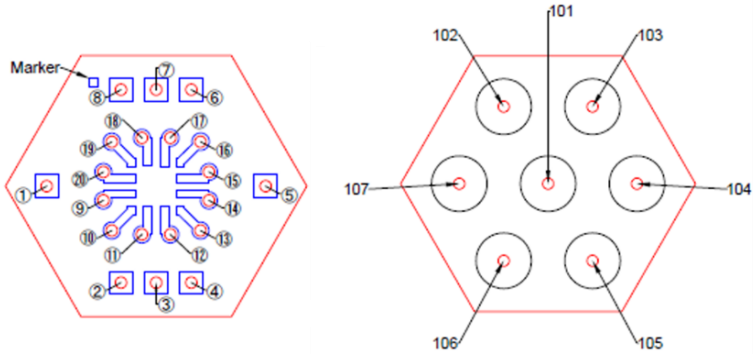


| | |
|---|---|
| NET1 (vdd) | ①,⑤,⑩ |
| NET2(C1) | ②,⑧,⑪ |
| NET3(C2) | ③,⑦,⑫ |
| NET4(gnd) | ④,⑥,⑬,⑲ |
| NET5 | ⑮,101 |
| NET6 | ⑱,102 |
| NET7 | ⑰,103 |
| NET8 | ⑯,104 |
| NET9 | ⑭,105 |
| NET10 | ⑨,106 |
| NET11 | ⑳,107 |
| Marker | Not connect |

**Figure 3.3** The layout of the ceramic substrate

### 3.1.3 The CMOS system

The stimulation function in the retinal device should be able to select stimulating electrodes and generate stimulating currents with desirable values that could depict the target object in phosphine matrix and different stimulation thresholds that variated in the patient. Thus, the CMOS system was employed in our retinal device to satisfy the stimulation requirements. The CMOS chip was fabricated using 0.35 μm standard process with a size of 500 × 500 $\mu m^2$, and a 5-volt DC-power drove it to generate the biphasic cathodic-first pulses in a maximum range of ± 1.55 mA with two power supplies (VDD and GND) and two signal controls (CONT 1 and CONT 2) inputs. The specifications of the CMOS chip are shown in Figure 3.4 (a). A

logical circuit in the CMOS chip is composed of a control circuit, a current generation circuit, and an electrode switching circuit. The operation function of the CMOS chip was controlled by two control signals (control signals 1 and 2) in conjunction with the control circuit and the current generation circuit to define the current values, and the final stimulating current was fed to the selected electrode by means of the electrode switching circuit. The block diagram for the CMOS operation is shown in Figure 3.4 (b). The CMOS chip not only allowed precise allocation of electrical signals to the selected electrodes to depict an objective as a phosphene matrix, but also significantly reduced the wiring number of interconnects. For instance, in Fig. 1, 49 electrodes normally required 49 interconnects to control the electrical stimulation. With the CMOS system, the number of interconnects was only four to control the 49 electrodes. Therefore, the proposed honeycomb-type retinal device with a CMOS system is a promising device structure for retinal implantation.

(a)

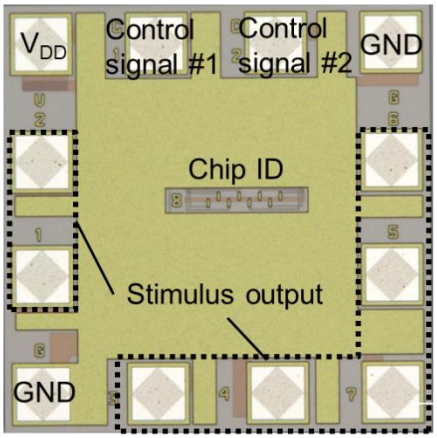


| Specification of the CMOS chip | |
|---|---|
| Fabrication | 0.35 um CMOS process |
| Supply voltage (V) | 5.0 (DC power) |
| Input number (N) | 4 |
| Output number (N) | 7 |
| Stimulating mode | Constant biphasic pulse |
| Stimulating current (mA) | ±1.55 |
| Microchip size (μm) | 500 × 500 |

(b)

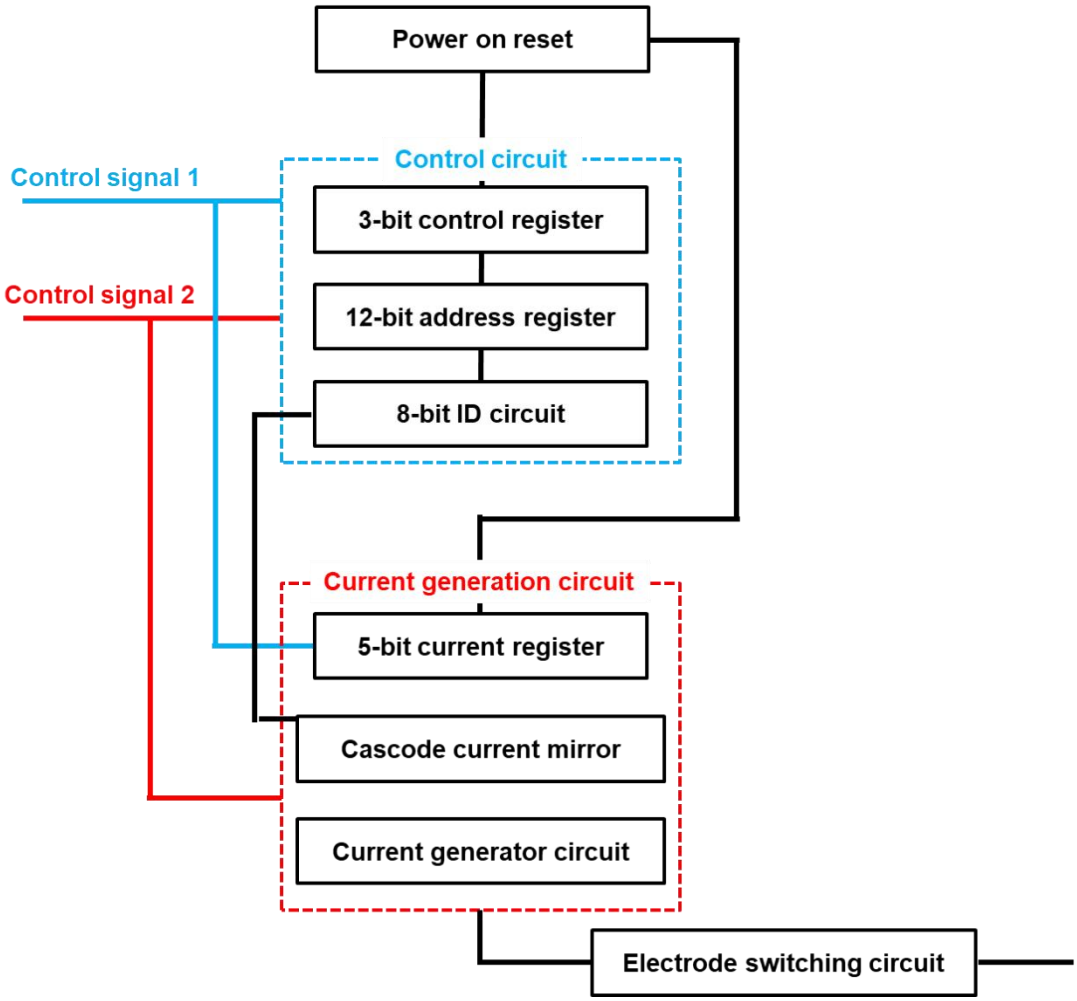


**Figure 3.4** The specification and block diagram of the CMOS chip

### 3.1.4 Platinum interconnections

The interconnect design is based on the pads and CMOS system. The width and thickness of the interconnects are 270 and 1.6 μm, respectively. The interconnect number could be tremendously reduced due to the pads on the ceramic and CMOS system; therefore, interconnect fabrication can be more feasible in developing the larger modules. For example, in Figure 3.5, with the special pads arrangement and CMOS system only four interconnects are required not only in 1 module (one ceramic substrate) but also in 7 modules (seven ceramic substrates). The four interconnects are VDD, GND, CONT1, and CONT2, respectively. With those four interconnects, the input source of power supply and signal control can drive the CMOS chips in individual modules. As a result, this interconnect layout is a promising design in case of larger modules. The interconnect material was also selected in platinum due to the distinct biocompatibility in platinum which is the same purpose as mentioned earlier. Hence, the primary component of the honeycomb-type retinal prosthesis device is mainly used in biocompatible material to strictly satisfy the requirement of implantable bioelectronics.

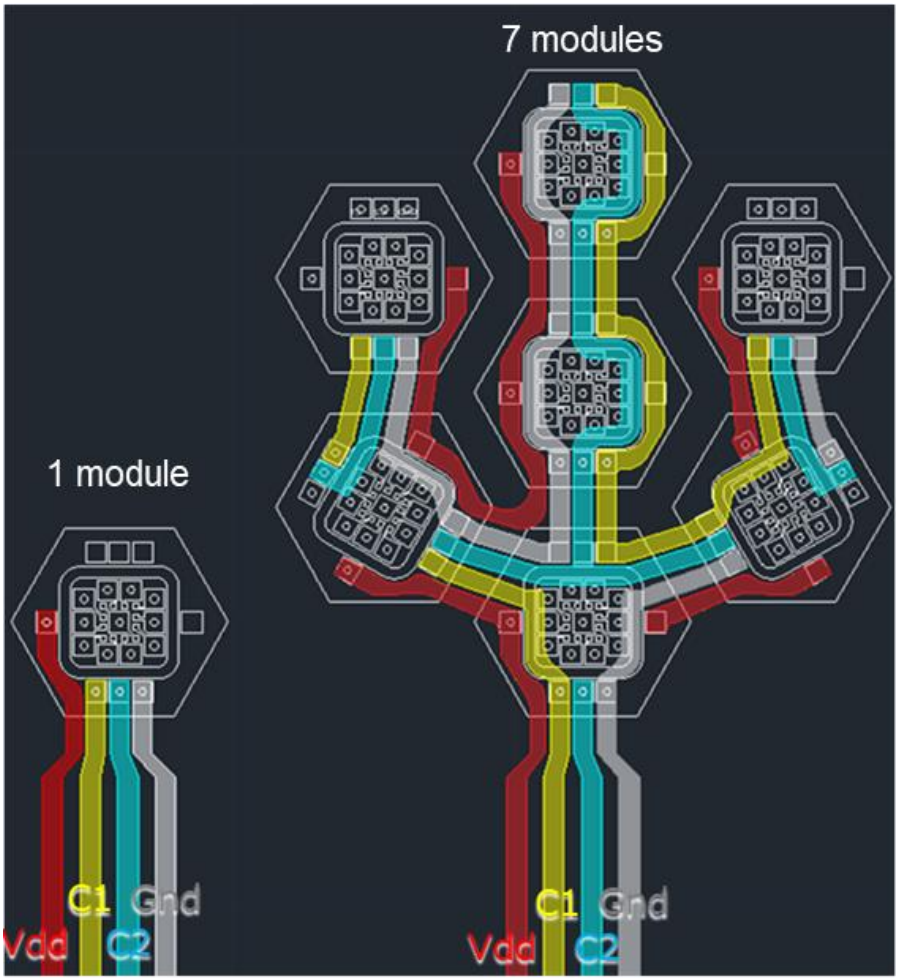


**Figure 3.5** The interconnects layout in 1 and 7 modules

### 3.1.5 Stimulating electrodes

For electrical neuro-stimulation, iridium oxide provides a higher charge storage/delivery capacity compared to that of Pt, PtIr, and TiN [15-18]. Thus, we fabricated an iridium oxide electrode on the Pt electrodes of the ceramic substrate to obtain excellent electrochemical performance. This research introduced a unique solution-based process, chemical bath deposition (CBD), to synthesize the iridium oxide film as the stimulating electrodes. In addition,

we also utilized the most common process, sputtering deposition, to produce the iridium oxide thin film in the MEMS process for comparison purposes.

3.1.5.1 Chemical bath deposition of iridium oxide thin film

The chemical bath deposition (CBD) process was adopted to fabricate an iridium oxide electrode. The CBD process was performed at room temperature without using a high-vacuum system to fabricate the iridium oxide, such as the sputtering process, therefore facilitating a facile process for depositing iridium oxide. Moreover, the CBD process can provide a uniform coating due to a solution-based process that could potentially be employed in 3-dimensional substrates and microstructures to obtain a conformal interface.

The deposition bath was composed of 3.4 mM potassium hexachloroiridate (Wako, Japan), 3.4 mM potassium sodium tartrate (Wako, Japan), 0.1 M sodium hydroxide (Wako, Japan), and 0.4 M sodium hypochlorite (5% min, Fujifilm, Japan), which respectively served as the Ir precursor (Ir ion source), chelating agent, pH adjuster, and oxidizing agent. Initially, potassium hexachloroiridate was dissolved in deionized water and aged for 24 h. Next, the potassium sodium tartrate solution was added to chelate the Ir ions to prevent the precipitation of $Ir^{3+}$ into an undesirable iridium oxide cluster. Third, a pH adjustor was added to adjust the pH to approximately 13. Sodium hypochlorite was added to oxidize the Ir ions to initiate the deposition of the iridium thin film on the patterned ceramic substrate. Each deposition process was conducted at 25 °C for 80 min. The thickness of the iridium oxide thin film for each

deposition bath is around 37 nm confirmed by SEM. The respective chemicals and concentrations are listed in Table 3.1.

**Table 3.1** The formula for chemical bath deposition of iridium oxide

| Chemicals | Function | Concentration (M) | Volume (ml) |
|---|---|---|---|
| $K_3IrCl_6$ | Ir ion source | 0.01 | 3.3 |
| Sodium potassium tartrate | Complexing agent | 0.01 | 3.3 |
| NaOH | pH adjustor | 1 | 1 |
| NaClO | Oxidizing agent | 12 wt% (min: 5%) | 2 |

In the CBD process, the iridium oxide is not selectively deposited on the electrode area (platinum electrode area). Due to a stronger adhesion and preferable growth between the iridium oxide and ceramic substrate, the iridium oxide would relatively intend to deposit on the ceramic substrate. Therefore, the ceramic substrate should be patterned a mask layer, such as photoresist or chemical-inert film, to prevent the iridium oxide film from directly depositing on the undesirable area, followed by a lift-off process to remove the patterned mask layer to obtain patterned iridium oxide electrodes finally.

A photolithography process was conducted to fabricate the patterned mask layer on the ceramic substrate. A positive photoresist (OAP and OFPR-8600) was used for the photolithography process. Noteworthy, the electrodes that are distributed on the edge of ceramic substrate are hardly coated with a conformal photoresist layer during the spin-coating

process. To overcome this problem, the extra substrates (same size of ceramic substrates) were surrounded the ceramic that needs to be patterned photoresist, as shown in Figure 3.6. The detailed parameter of the photolithography process is listed in Table 3.2.

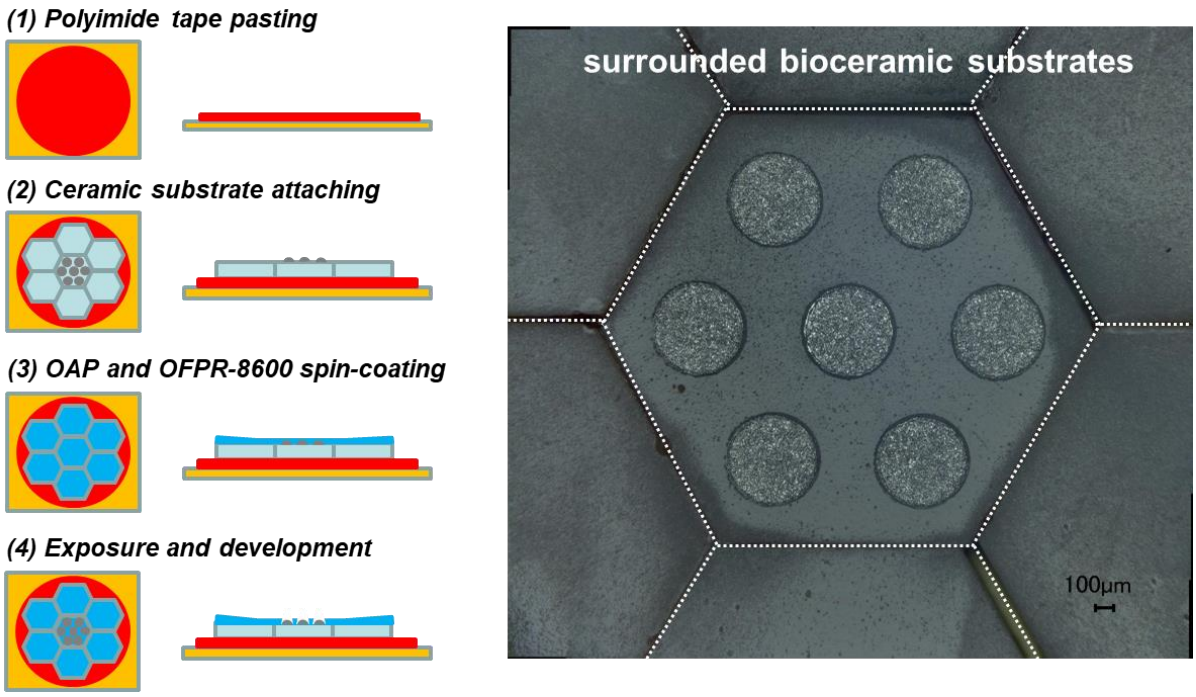


**Figure 3.6** The sample preparasion for photolithgraphy process.

**Table 3.2** The parameter of photolithography process

| | | | |
|---|---|---|---|
| Photoresist coating | Pre-baking | 150 ℃ (hot plate) | 5 min |
| | HDMS treatment (OAP coating) | $1^{st}$ : 500 rpm<br>$2^{nd}$ : 4000 rpm | 5 sec<br>20 sec |
| | Soft-baking | 110 ℃ (hot plate) | 1 min |
| | OFPR8600 coating | $1^{st}$ : 500 rpm<br>$2^{nd}$ : 4000 rpm | 5 sec<br>20 sec |
| | Pre-baking | 110 ℃ (hot plate) | 1.5 min |
| Photoresist patterning | Exposure | MA-10, MIKASA | 5 sec |
| | Development | NMD-3 | 1 min |
| | Rinsing | Deionized water | 30 sec |
| | $N_2$ dry out | | |
| | Post-baking | 130 ℃ (hot plate) | |

While the patterned photoresist was completed on the ceramic substrate, the patterned ceramic substrate was immersed into the chemical bath to deposit the iridium oxide thin film. However, the patterned photoresist easily peeled off or dissolved during the chemical bath deposition of the iridium oxide thin film, which is deposited on the ceramic substrate and non-uniform film coating as shown in Figure 3.7. It is possible owing to unexpected chemical reactions occurred from the photoresist and chemicals in the deposition bath.

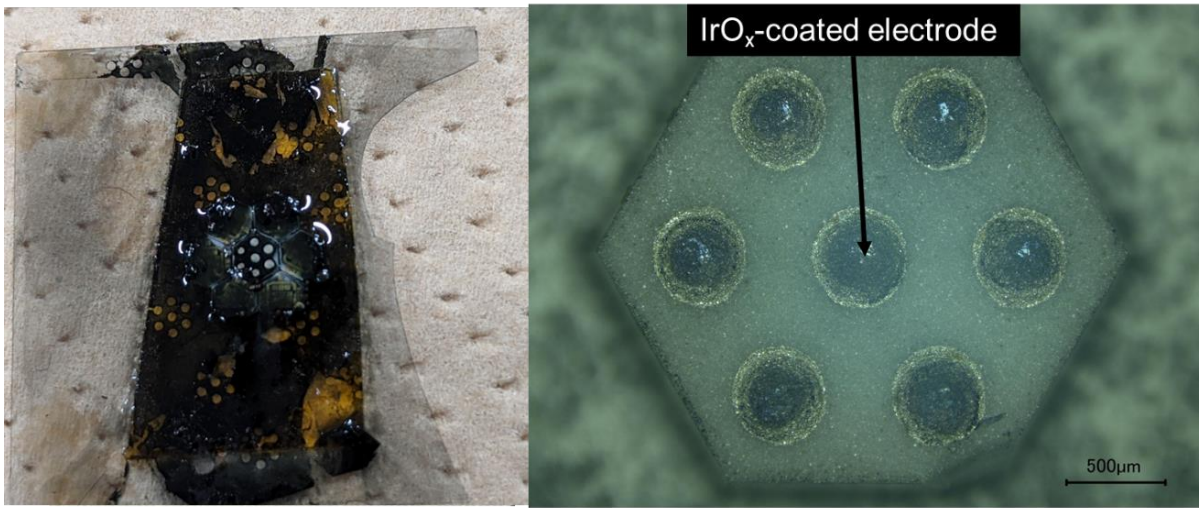


**Figure 3.7** The photographs of the CBD-derived iridium oxide thin film on a ceramic substrate by using a photoresist pattern

Thus, we used the chemical-inert material as a patterned mask to ensure that the mask layer is stable in the chemical bath to deposit the iridium oxide thin film. A parylene is a suitable chemical-inert material for the patterned mask due to the conformal coating and to be easily patterned by laser ablation or $O_2$ plasma.

First, parylene was spun on the ceramic substrate for use as a chemically inert mask for further CBD processes (PDS2010, Specialty Coating Systems, USA), as shown in Figure 3.8 (a), followed by a high-precision laser system (Q-switched Nd: YAG laser, $\lambda = 266$ nm) and $O_2$ plasma with 50 W in 10 ml $min^{-1}$ $O_2$ flow for 30 s (Model FA-1, Samco, Japan) to ablate the parylene to obtain an exposed area for the iridium oxide fabrication, as shown in Figure 3.8 (b). Next, iridium oxide was deposited on the exposed Pt area of the ceramic substrate via immersing the whole sample in a deposition bath. The parameter of parylene coating and patterning is listed in Table 3.3.

**Table 3.3** The parameter of the parylene patterning on ceramic substrate for CBD-iridium oxide film

| Process | Equipment | Parameter | |
|---|---|---|---|
| Parylene coating | PDS 2010 | Dimer: 4 g | |
| | | Pressure: 35 mTorr | |
| | | Thickness: ~2 μm | |
| Parylene patterning | VL-C30 | Magnitude: 20 x | |
| | | Slit size:<br>X = 1000, 500; Y = 1000, 500 | |
| | | Wavelength: 266 nm | |
| | | Energy: 1000 | |
| Laser-induced carbon ablation | FA-1 | $O_2$ flow rate: 10 ml/min | 1 min |
| | | Pressure: 10 Pa | |
| | | RF power: 50 W | |

To obtain a sufficient thickness of iridium oxide film (220 nm), the processes were repeatedly carried out in six batches. Due to the layer-by-layer deposition, adequate heat treatment to improve the adhesion among the layers and interface of platinum is needed. The parameter of the heat treatment is at 150 ℃ in the air for 30 min. While the first layer of the

iridium oxide thin film is deposited, the sample is required to carry out the heat treatment to increase the adhesion between the first layer of the iridium oxide film and platinum electrode. Afterward, the heat treatment was conducted every two deposition baths. After six bathes, the YAG laser and $O_2$ plasma were used to remove the parylene mask and define the exposed iridium oxide area in the hexagonal-arrangement electrode array as shown in Figure 3.8 (c). The overview process is shown in Fig. 3.9 (a-b).

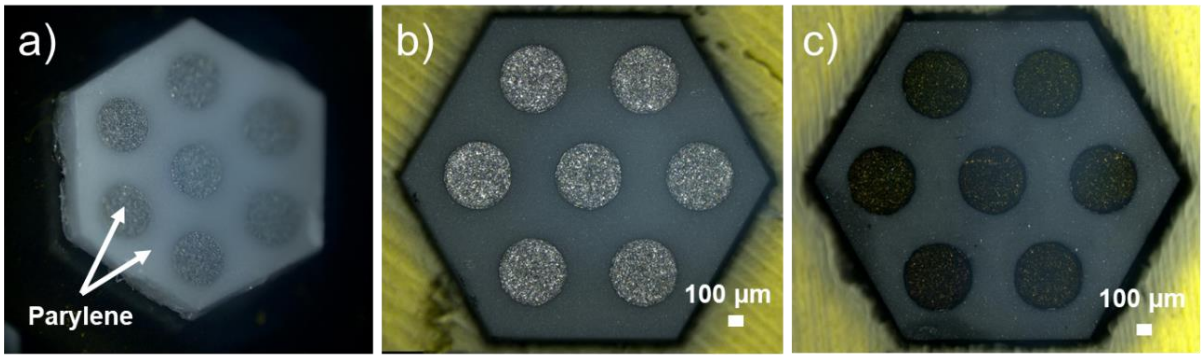


**Figure 3.8** The photographs for ceramic substrate of (a) parylene coating, (b) parylene ablation on electrodes, and (c) chemical bath deposition of iridium oxide thin film on the platinum electrodes.

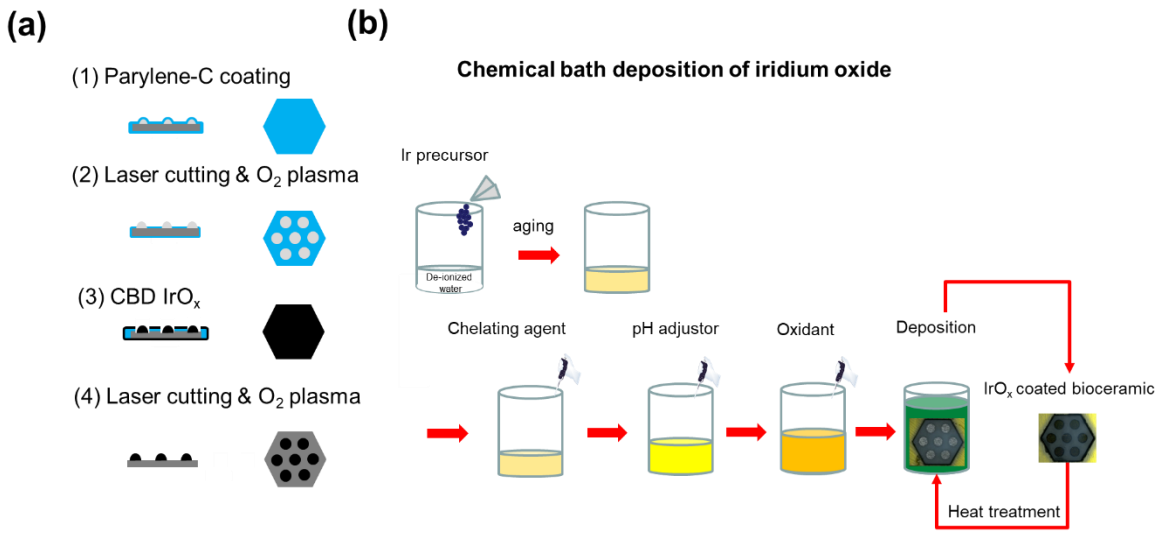


**Figure 3.9** The fabrications of iridium oxide electrodes in (a) CBD process, and (b) the chemical bath preparation

### 3.1.5.2 Sputtering deposition of iridium oxide electrodes

The sputtering process is the most commonly used method for fabricating iridium oxide, and it has been widely developed and used in the MEMS process for stimulating electrode application. Thus, we also prepared the sputtering deposition process to fabricate iridium oxide as the bio-stimulating electrode on top of the ceramic substrate as a comparison with CBD-derived iridium oxide.

The parameter of the sputtering deposition such as the flow rate of argon and oxygen, and partial pressure of oxygen is a critical factor to a stoichiometry of deposited iridium oxide thin film, which is highly related to final electrode performances. In this research, we investigated the sputtering parameter for the deposition of iridium oxide to obtain the best performance. All the sputtering samples that to be optimized are deposited on the $SiO_2$ wafer, and the thin film structure is composed of a 50 nm titanium (adhesive layer) and the iridium oxide by using a 200 W RF-generator sputtering machine (CFS-4ES-II, Shibaura, Japan). The structure of the iridium oxide thin film sample is shown in Figure 3.10. The indicator to the optimized parameter for the iridium oxide thin film is using cyclic voltammetry (CV) to realize a cathodic charge storage capacity (CSCc) of the iridium oxide thin film in various sputtering parameters.

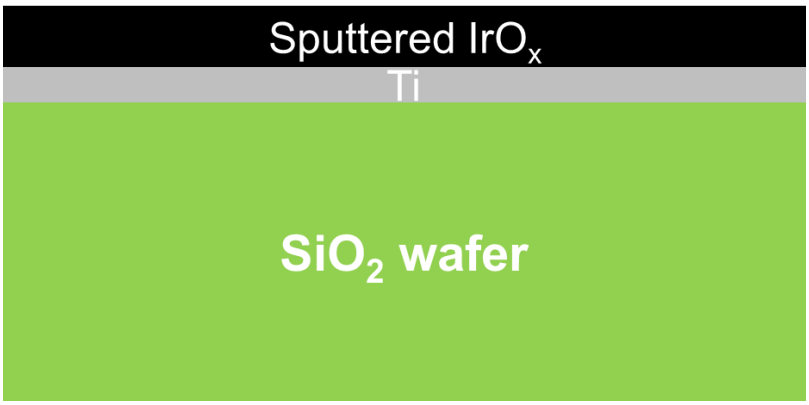


**Figure 3.10** The structure of the iridium oxide thin film sample

The CV was conducted using a potentiostat/galvanostat (PGSTAT204, Metrohm Autolab, Netherlands) in a three-electrode setup, as shown in Figure 3.11. A working electrode is the sputtered iridium oxide thin film in an area of 0.264 cm$^2$, a countering electrode is a platinum foil (2 × 3 cm$^2$), and a reference electrode is Ag|AgCl (3 M).

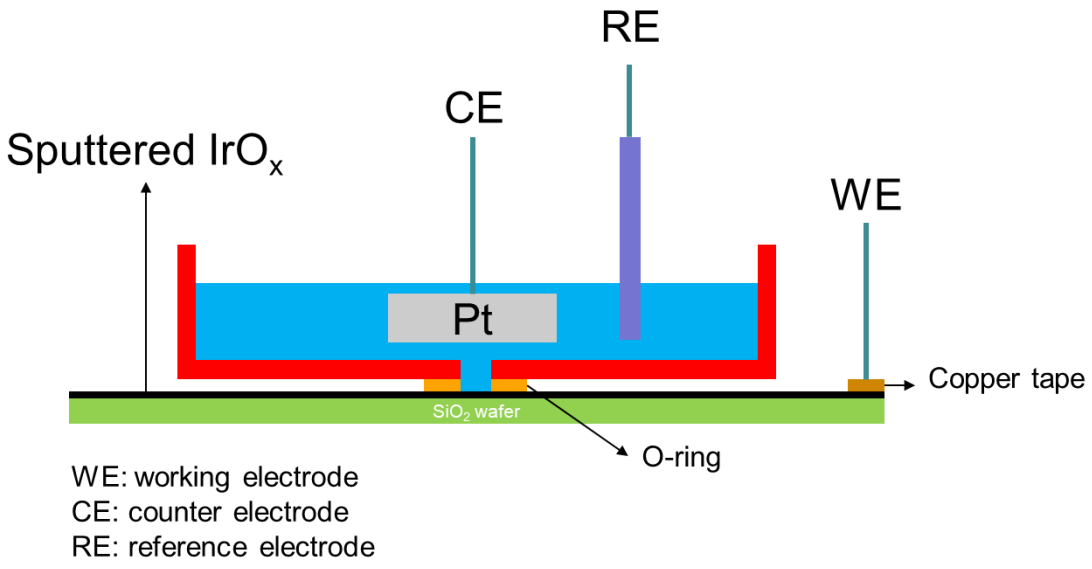


**Figure 3.11** The CV measurement setup for optimizing sputtered iridium oxide thin film

The CV measurement is to calculate the cathodic charge storage capacity (CSCc), which is determined by the integration of cathodic current in a potential range between -0.6 and 0.8 V (water window) at a scan rate of 50 mV $s^{-1}$, and the total columbic charge was divided by the scan rate and the electrode area, as shown in an equation (1). The CSCc value indicates that the electrode was able to deliver the stored charge for neuron stimulation.

$$CSCc = \frac{1}{vA}\int_{Ec}^{Ea} |i|\, dE \quad (1)$$

where v is the voltage scan rate (V $s^{-1}$), A is the exposed area of the working electrode ($cm^2$), Ea and Ec are the maximum anodic and cathodic voltages versus Ag|AgCl (V), respectively, and *i* is the measured current of the working electrode (A).

The CSCc value is proportional to the thickness of iridium oxide film, and it is due to the more materials that could store the electrical charge via different chemical-states of iridium such as the redox reaction (faradaic reaction) as shown in the following equation (1),

$$Ir^{3+} \rightleftarrows Ir^{4+} + e^- \quad (1)$$

Therefore, the thickness factor should be considered to investigate the optimized sputtered parameter for deposition of the iridium oxide film.

The flow rate of argon was constantly fixed at 5 sccm and mixed with different flow rates of oxygen in a ratio of 1:4 and 1:2. The partial oxygen pressure was adjusted by working pressure in the sputtering chamber. To understand the optimized parameters for iridium oxide

thin film, we normalized the electrochemical performance in various sputtering parameters in CSCc/thickness as a function of partial oxygen pressure as shown in Figure 3.12. As a result, Figure 3.12 shows that the CSC/thickness value increases with the oxygen flow rate and partial pressure of the oxygen. It indicates that the sputtered iridium oxide film with a higher $O_2$ flow rate appears a higher normalized charge storage capacity (CSCc/thickness). As mentioned earlier, the charge storage mechanism is via different chemical states of iridium atoms, and the most stable redox reaction of iridium atoms is between 3+ and 4+. Accordingly, the amount of oxygen should be enough to oxidize the iridium atoms into iridium oxide so that the oxidized iridium atoms could storage more electrical charges to achieve the highly efficient neural stimulation. The turning point in CSC/thickness as a function of partial oxygen pressure is at 0.9 Pa. If the partial oxygen is less than 0.9 Pa, the iridium atoms remained in a metallic state and formed a metallic iridium thin film, leading to a non-redox reaction that occurred in CV measurement. The normalized CSCc value is slightly lower while using larger than 0.9 Pa of partial oxygen pressure. It is possible due to a metallic iridium target to be corroded under the higher partial oxygen pressure (> 0.9 Pa) that formed the iridium oxide layer at the surface of the metallic iridium target, leading to less bombarded iridium ion that deposited on the substrate.

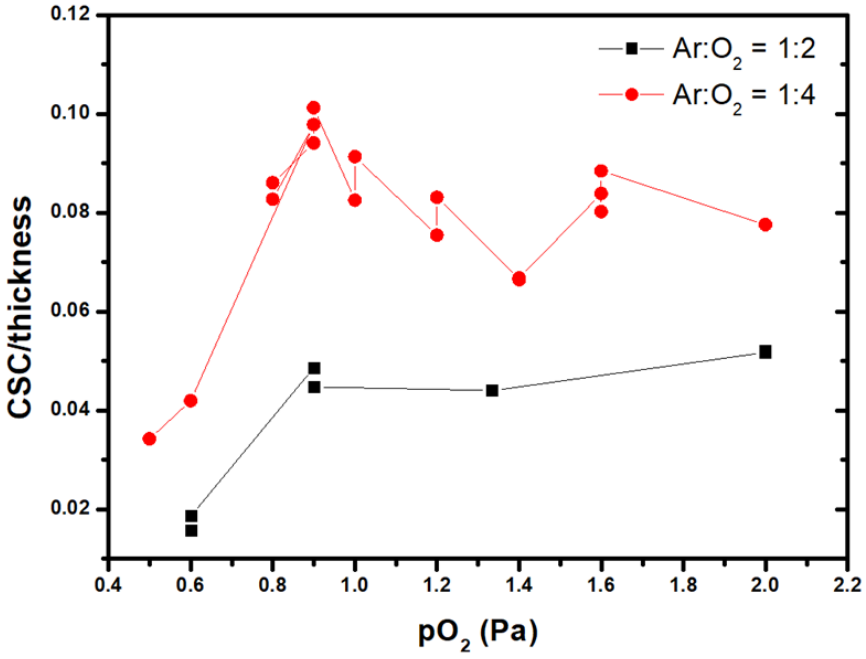


**Figure 3.12** The CV measurement setup for optimizing sputtered iridium oxide thin film

After optimizing the sputtering parameter for deposition of the iridium oxide thin film. To achieve the same purpose as the patterned electrodes, photolithography was conducted with using the OAP, OFPR-8600 photoresist and NMR-3 developer (Tokyo Ohka Kogyo Co., LTD., Japan), contact-mode mask aligner (MA-10, Mikasa, Japan), and PG-remover (Chemo, USA), the photolithography process is identical to the previous process as shown Figure 6. While the patterned photoresist finished on the ceramic substrate, a 50 nm titanium (adhesive layer) and 630 nm iridium oxide were carried out using a 200 W RF-generator sputtering machine (CFS-4ES-II, Shibaura, Japan). The sputtering parameters for Ti is under 0.6 Pa in Ar (20 sccm), and for the iridium oxide is under 1.125 Pa in Ar (5 sccm) and $O_2$ (20 sccm). The flowchart and sputtering parameter for fabrication of sputtered iridium oxide electrodes on ceramic substrate are shown Figure 3.13 and Table 3.4.

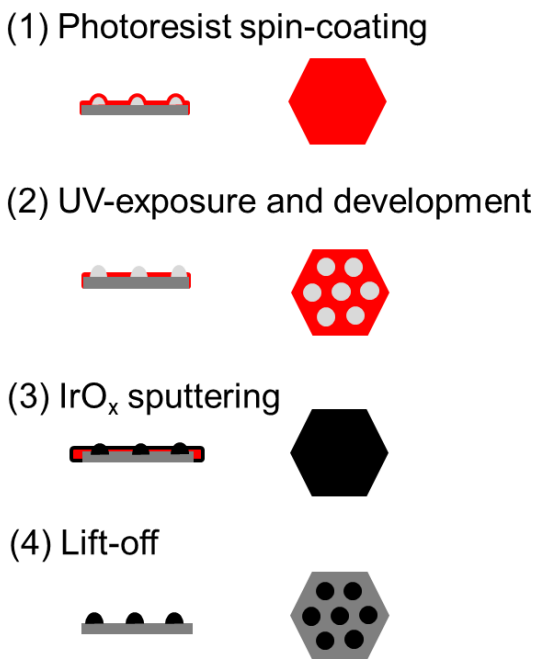


**Figure 3.13** The flowchart for sputtering iridium oxide electrodes

**Table 3.4** The sputteting parameter for iridium oxide electrodes

| | Parameter | Thickness |
|---|---|---|
| Reverse sputtering | Atmosphere: Ar gas | |
| | Gas flow rate: 10 sccm | |
| | Sputtering time: 1 min | |
| | RF power: 50 W | |
| Ti sputtering | Atmosphere: Ar gas | 50 nm |
| | Gas flow rate: sccm | |
| | Sputtering time: 8.2 min | |
| | RF power: 200 W | |
| IrOx sputtering | Atmosphere: Ar and $O_2$ | 630 nm |
| | Gas flow rate:<br>5 sccm for Ar; 20 sccm for $O_2$ | |
| | Sputtering time: 15 min | |
| | RF power: 200 W | |

### 3.1.6 Assembly of the retinal device

While the iridium oxide electrodes were completely deposited on the ceramic substrate, the iridium oxide-coated ceramic substrate are ready for device assembly. Figure 3.14 shows a fabrication the retinal prosthesis device. The assembly steps are further discussed as follow.

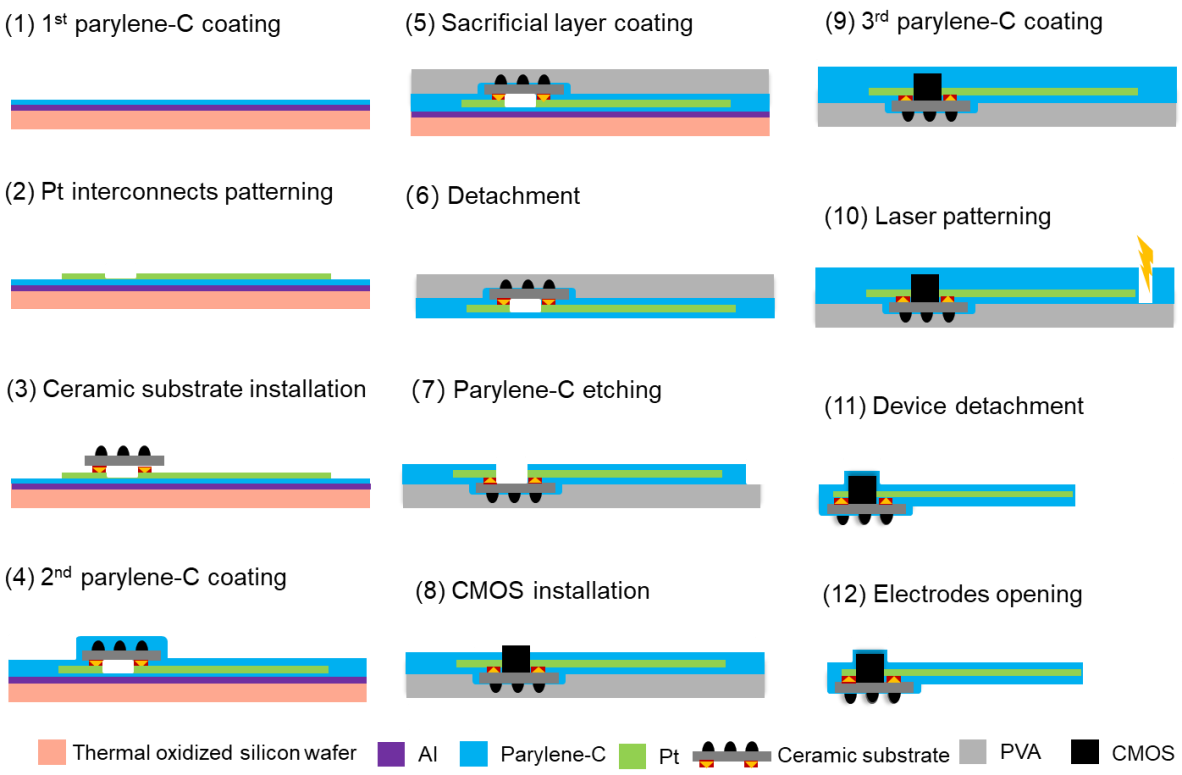


**Figure 3.14** The flowchart of retinal device fabrication

**Step 1: 1st parylene layer coating**

A thermal oxidized silicon substrate (TOS) was used as the supporting substrate for processing the device assembly. First, the TOS was respectively immersed in acetone and isopropanol solution at 35 ºC for 10 min, followed by an $O_2$ plasma etching with 50 W in 10 ml $min^{-1}$ $O_2$ flow for 5 min in purpose of cleaning the containment at the TOS surface.

Subsequently, an aluminium layer was coated on the TOS substrate using evaporation deposition (VPC-260F, ULVAC) to serve as the sacrificial layer. Next, the first layer of parylene in thickness of 5 µm by using chemical vapour deposition (PDS2010 Specialty Coating Systems, USA) was deposited on top of the aluminium layer. The first layer of parylene was used as a main substrate for supporting the retinal device and interconnects. The deposition condition for parylene is listed in Table 3.5.

**Table 3.5** The deposition condition of the parylene layer for device assembly process

| | Equipment | Parameter |
|---|---|---|
| Parylene coating | PDS 2010 | Dimer: 10 g |
| | | Pressure: 35 mTorr |
| | | Thickness: ~5 µm |

**Step 2: Pt interconnects patterning**

To fabricate the 4 interconnects for the VDD, GND, CONT1 and CONT2 wiring, we selected platinum as the interconnect material, because it is more non-cytotoxic concerns as compared to Au interconnects. The Pt interconnects with 240 µm width and in pitch of 310 µm were patterned on the first parylene layer by means of photolithography and sputtering process, as shown in Figure 3.15.

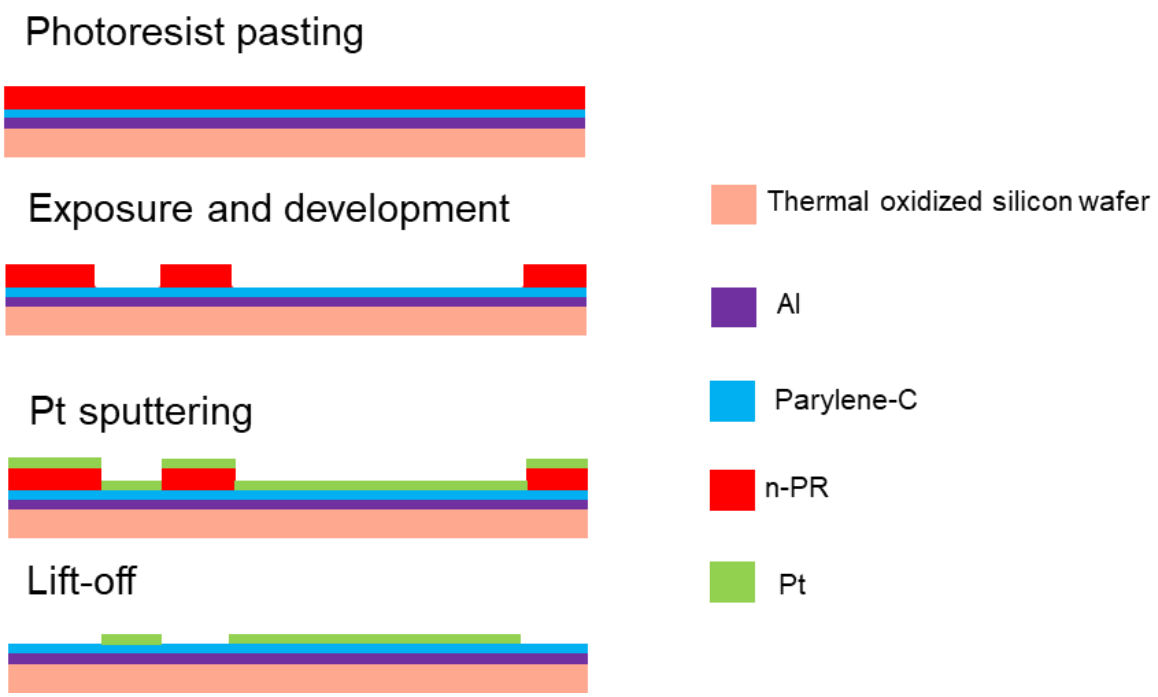


**Figure 3.15** The detailed flowchart for platinum interconnects patterning

At first, the $O_2$ plasma was conducted not only to clean the possible containment on the surface of the 1st parylene layer but also to improve the adhesion for the photoresist patterning process. The parameter of $O_2$ plasma here is identical to Table 3.4. After $O_2$ plasma treatment, the negative-type photoresist (n-PR; RY3315EE) was pasted by a heat roller (L3570HI, Asmix) at 125 ºC to complete the photoresist pasting on the 1st layer of parylene. Then, the final platinum interconnects were successfully fabricated via the photolithography and sputtering process as shown in Figure 3.16. The sputtering parameter for the platinum interconnects is listed in Table 3.6.

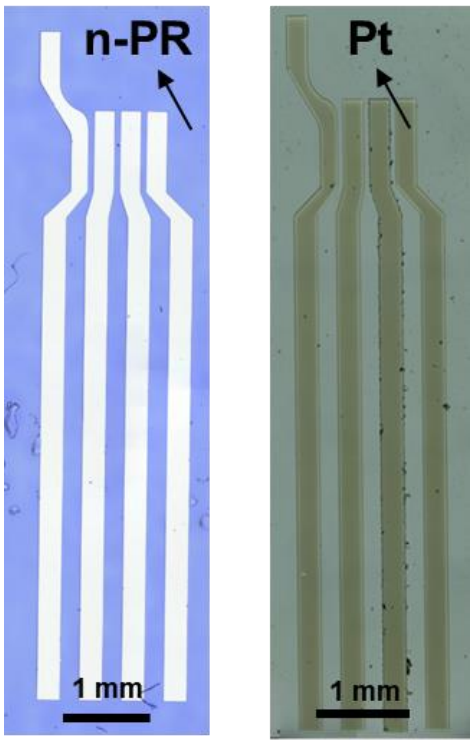


**Figure 3.16** The photographs of the patterned photoresist (left), and the final platinum interconnects (right)

**Table 3.6** The sputteting parameter for platinum interconnects

| | Parameter | Thickness |
|---|---|---|
| Reverse sputtering | Atmosphere: Ar gas | |
| | Gas flow rate: 10 sccm | |
| | Sputtering time: 1 min | |
| | RF power: 50 W | |
| Ti sputtering | Atmosphere: Ar gas | 50 nm |
| | Gas flow rate: 20 sccm | |
| | Sputtering time: 8.2 min | |
| | RF power: 200 W | |
| Pt sputtering | Atmosphere: Ar and $O_2$ | 1.6 µm |
| | Gas flow rate: 20 sccm | |
| | Sputtering time: 80 min | |
| | RF power: 200 W | |

**Step 3: Ceramic substrate installation**

Next, the ceramic was mounted on the platinum interconnects by using a flip-chip bonding process (M-90, HiSol). To correctly place the bioceramic substrate on the platinum interconnects, the bonding position is around 1.0014 mm upper from the edge of the third platinum interconnect (CONT2). A schematic diagram is shown in Figure 3.17. The ceramic substrate was assembled on Pt interconnect lines with an anisotropic conductive paste (TAP0402E, Kyocera, Japan) under 12 N pressure at 130 ºC for 15 s. After the ceramic substrate flip-chip bonding, polyvinyl alcohol (PVA) was used as the sacrificial layer, and was coated on the electrode surface to prevent the second layer of the parylene from directly depositing on the electrodes.

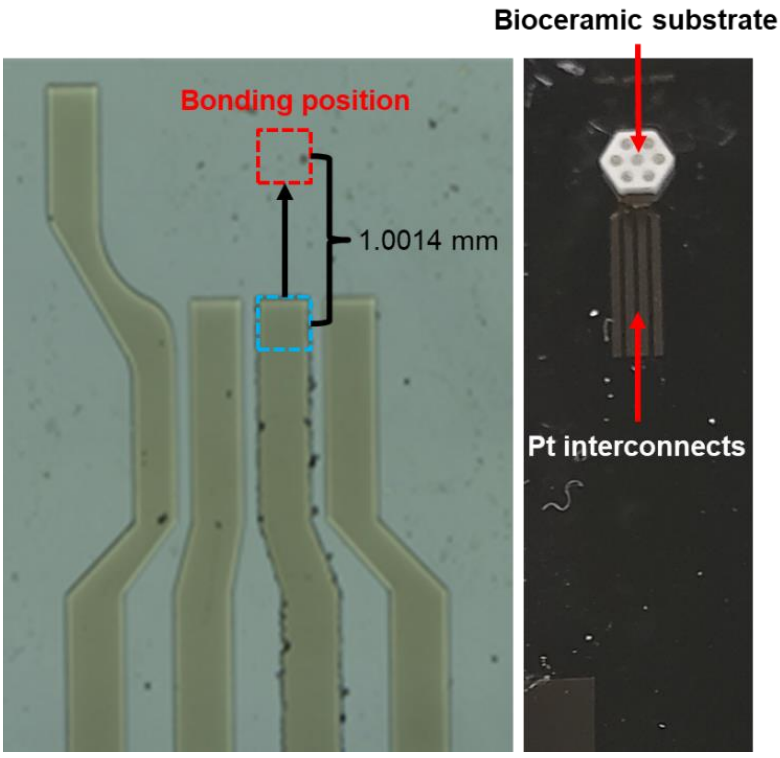


**Figure 3.17** The schematic diagram for flip-chip bonding position

**Step 4: 2nd parylene layer coating**

Next, the second layer of the parylene was deposited to encapsulate the platinum interconnects. Before the parylene encapsulation, the platinum interconnects and the first layer of the parylene was immersed in a silane solution (DuPont Toray Specialty Materials Kabushiki Kaisha, Japan) at 25 ºC for 15 min to enhance the adhesion between two layers of the parylene. The preparation condition for the silane coupling solution is listed in Table 3.7.

**Table 3.7** The preparation condition for silane coupling solution

| | | |
|---|---|---|
| Silane coupling solution (XIAMETER_OFS-6030) | Volume ratio of Silane:DIW:IPA = 0.55 100: 10 | Stirring over 2 hours |
| | Immersing time | 15 min |
| | Directly dry out by $N_2$ gas | |
| | Further dry out in oven at 60 ºC | 30 min |

**Step 5 and 6: Sacrificial layer coating and detachment**

For CMOS chip installation, a sacrificed acrylic substrate with the PVA layer was spun on top of the sample, and then the sample was detached from TOS by alkaline solution (2 M NaOH) to remove the aluminum sacrificed layer. At this stage, the whole sample is upside down

for the purpose of the CMOS chip installation. The sacrificed acrylic substrate with the PVA and the process in photographs are shown in Figure 3.18.

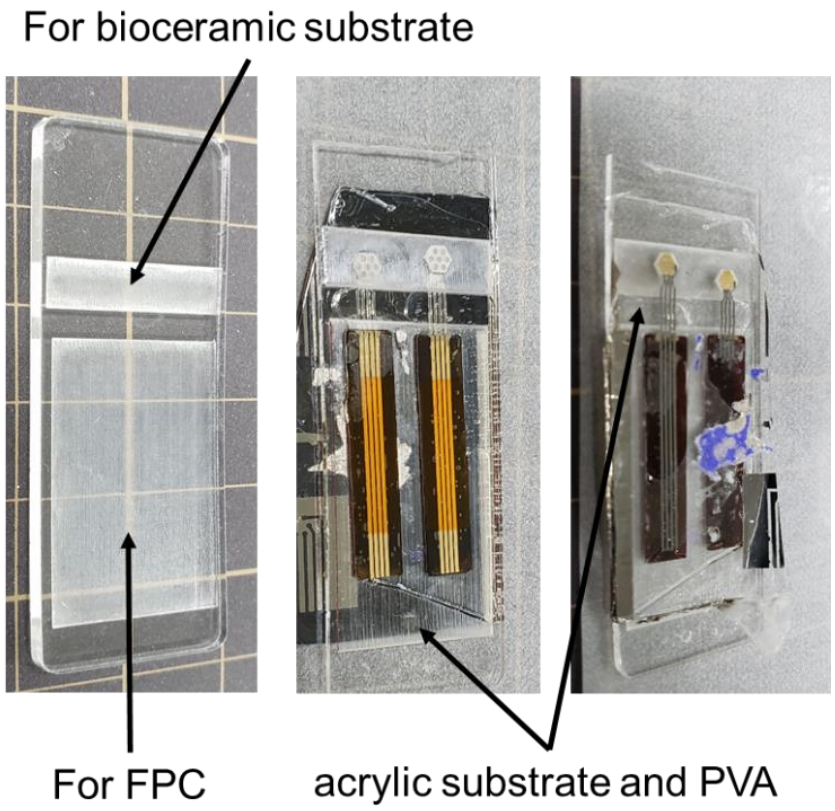


**Figure 3.18** The schematic diagram for sacrificial layer coating and detachment

**Step 7: Parylene etching for the CMOS chip installation**

Subsequently, the parylene layer on top of the pads was removed by YAG laser and O2 plasma for the CMOS installation. The parameter for parylene etching is the same as in Table 3.3.

**Step 8: CMOS chip installation**

Before the CMOS chip installation, in order to ensure an electrical connection for corresponding pads between the CMOS chip and the ceramic substrate, a gold bump was formed on the pads of the CMOS chip for a better electrical connection. The gold bumps were conducted by WEST-BOND (MODEL 770D series). After gold bumps formation, the leveling process for each was done by flip-chip bonder to obtain a sufficient connection area while CMOS chip installation. The final gold bumps on the CMOS chip and formation condition for gold bumps are shown in Figure 3.19 and Table 3.8, respectively. The CMOS chip installation also used a flip-chip bonding process to mount the CMOS chip in an accurate position, and the boning parameter is identical to ceramic substrate installation.

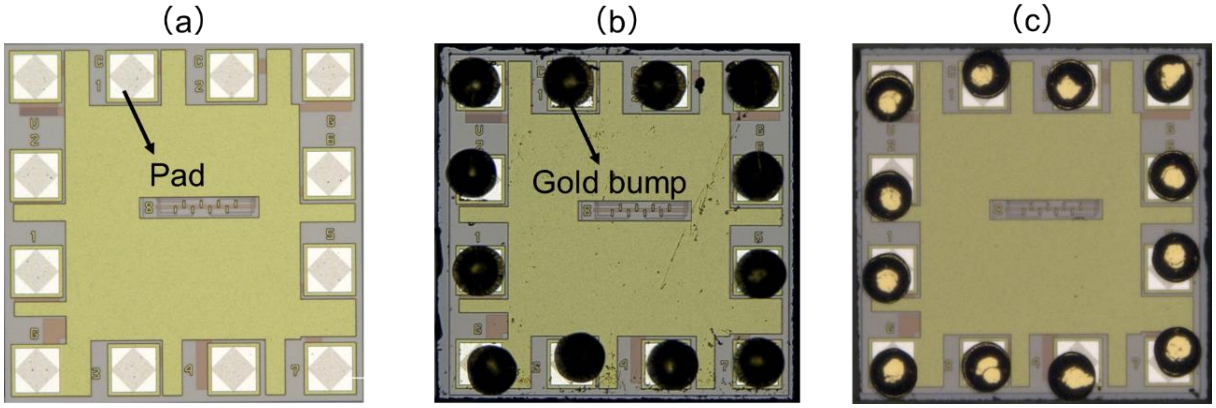


**Figure 3.19** The schematic diagram for sacrificial layer coating and detachment

**Table 3.8** The condition for gold bump formation

| | Equipment | Condition |
|---|---|---|
| Gold bump formation | MODEL 7700D series (WEST BOND) | Wireline: gold (diameter: 20 μm, TANAKA Precious Metals) |
| | | Capillary: 1572-15-625GM (GAISER) |
| | | Weight: 30 high |
| | | Ball size: 2.0 |
| | | Current: 3.5 |
| | | $P_w$: 170 |
| | | Formation time: 30 ms |
| | | Temperature: 200 ºC |

**Step 9: 3rd parylene layer coating**

After the CMOS flip-chip process, the third layer of the parylene was deposited for the CMOS chip encapsulation. The silane coupling treatment was also required to carry out before 3rd parylene layer coating due to adhesion improvement among the second and third layers of parylene. The condition for silane coupling and parylene layer coating is identical to step 4.

## Step 10 and 11: Laser patterning and device detachment

Next, the device structure was patterned and detached from acrylic substrate by YAG laser and acetone, respectively. The patterning condition and program are listed in Tables 3.9 and 3.10.

**Table 3.9.** The condition for laser patterning

| | Equipment | Condition |
|---|---|---|
| Laser patterning | VL-C30<br>(TNS system) | Magnitude: 20 x |
| | | Slit: X = 3000 μm, Y = 3000 μm |
| | | Wavelength: 266 nm |
| | | Shot frequency: 30 Hz |
| | | Energy: 1000 |

**Table 3.10** The programmable condition for laser patterning

| Program name | YAG レーザコントローラ v1.2 |
|---|---|
| Low speed | 110 |
| High speed | 50000 |

**Step 12: Electrodes opening**

Finally, to expose the electrodes for the neuron stimulation, the laser was used for patterning the parylene along with the edge of the ceramic substrate, followed by immersing into deionized water to dissolve the PVA layer to expose the electrodes array. The final device composed of 7 CBD-iridium oxide electrodes and 4 platinum interconnects embedded in the parylene is shown in Figure 3.20.

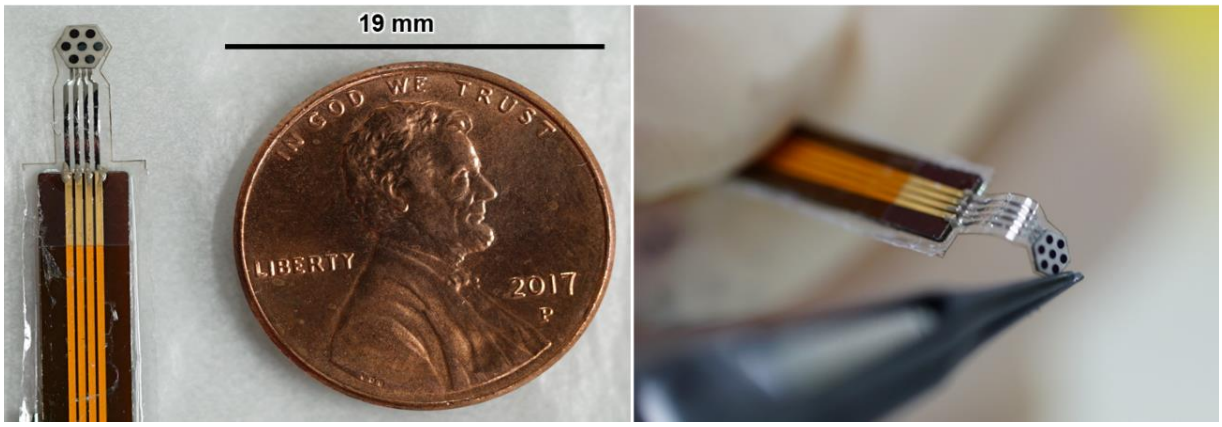


**Figure 3.20** The photographs for the final retinal prosthesis device

# 4. Results and discussion

## 4.1 Characterization of the stimulating electrodes

The electrode surface morphology was characterized by scanning electron microscopy (Keyence) with an accelerating voltage of 5 kV. X-ray photoelectron spectroscopy (ULVAC-PHI PHI 5000 VersaProbeII) was used to determine the chemical state of the iridium in the iridium oxide electrode.

Figure 4.1 shows the SEM images of seven CBD-iridium oxide electrodes with a diameter of 500 μm in a hexagonal arrangement. As shown in Fig. 4.1, the CBD-iridium oxide film was conformably deposited on the platinum electrodes as the final interface for neuron stimulation without any defective cracks. Moreover, the iridium oxide thin film was only deposited on the electrode area, because the iridium oxide is a conductive material so that the brighter area is only shown in the electrode area implying that the iridium oxide thin film was successfully deposited on the electrode area.

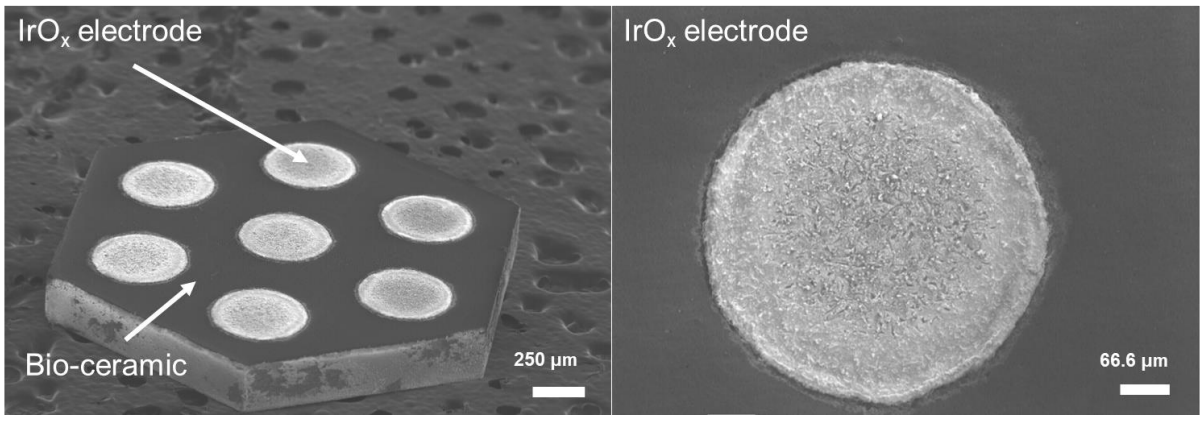


**Figure 4.1.** The SEM images of CBD-iridium oxide electrode array

To determine the chemical state of the iridium in the CBD-derived and sputtered iridium oxide, the surface information of the electrodes was investigated by XPS analysis. The XPS profiles of the CBD-derived and sputtered iridium oxide electrodes are shown in Fig. 4.2. Ir 4f XPS profile reveals that the natural chemical state of the CBD-derived and sputtered iridium oxide is $Ir^{4+}$ associated with the Ir $4f_{7/2}$ and $4f_{5/2}$ peaks at a binding energy of 62.2 and 65.2 eV, respectively [22]. XPS fitting for Ir 4f spectra shows only $Ir^{4+}$ peaks are fitted in the CBD and sputtered iridium oxide, indicating that the oxidation state of as-prepared iridium oxide films is 4+. It is noted that the nature of oxygen in the CBD-derived and the sputtered is different. The fitting peaks for O 1s profile are 530.5, 531.6 and 532.9 eV for lattice oxygen in iridium oxide (Ir-O-Ir), hydroxide group (Ir-OH), and water ($Ir-OH_2$), respectively [42]. Figure 4.2 (b) and (c) show the area of the peaks of Ir-OH in the CBD-derived iridium oxide thin film is larger than that of the sputtered iridium oxide thin film, indicating the hydroxide group is abundant at the surface of the CBD-iridium oxide thin film.

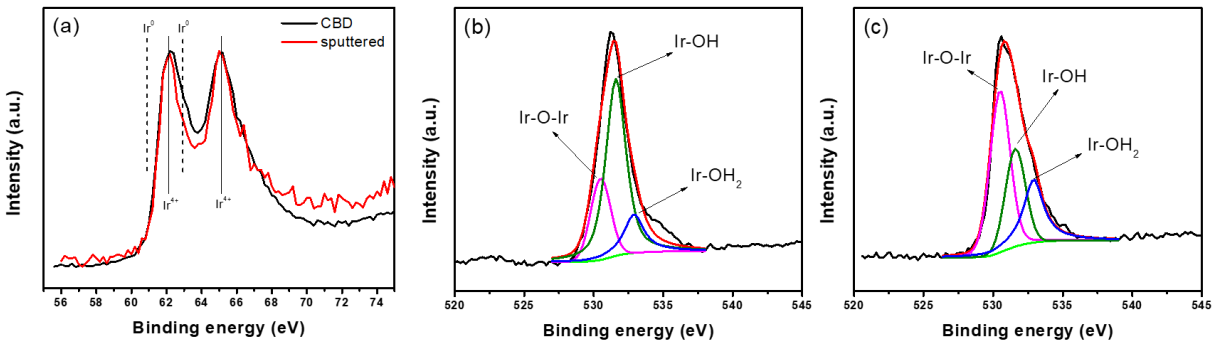


**Figure 4.2** The XPS profile for CBD and sputtered iridium oxide electrode. (a) Ir 4f spectra and O 1s profile of (b) CBD-derived, and (c) sputtered iridium oxide thin film

## 4.2 Electrochemical evaluation of the stimulating electrodes

For electrical neuron stimulation, the electrochemical properties of stimulated electrodes are critical for achieving efficient neuron stimulation and operation safety without any irreversible reactions such as water oxidation. Therefore, stimulated electrodes are required to assess their electrochemical performance in terms of charge storage capacity (CSC), CIC, and impedance response. The electrochemical performance of the electrodes was evaluated after a CV scan at 50 mV $s^{-1}$ for 500 cycles.

To evaluate the chemical properties of the stimulating electrodes, wire bonding to the individual electrodes is required. The corresponding pads to the electrodes are on the rear side of the ceramic so that the PCB (printable circuit board) is selected for the flexible version, which could be easily patterned. The wiring process in the graphic flowchart is shown in Figure 4.3. First, the PCB was pasted with polyimide tape and cut in a rectangle shape to open a space for wire bonding. Then, the ceramic was placed on the opened polyimide tape. At this stage, the ceramic substrate setting for wire bonding is completed. Next, the whole sample was upside down to place on the cover glass for aluminum wiring. Finally, the epoxy was used to seal the Al wirings to prevent the PBS solution from contacting the wiring. The heat treatment for solidification of the epoxy was at 110 ºC in the air in the oven for 20 min.

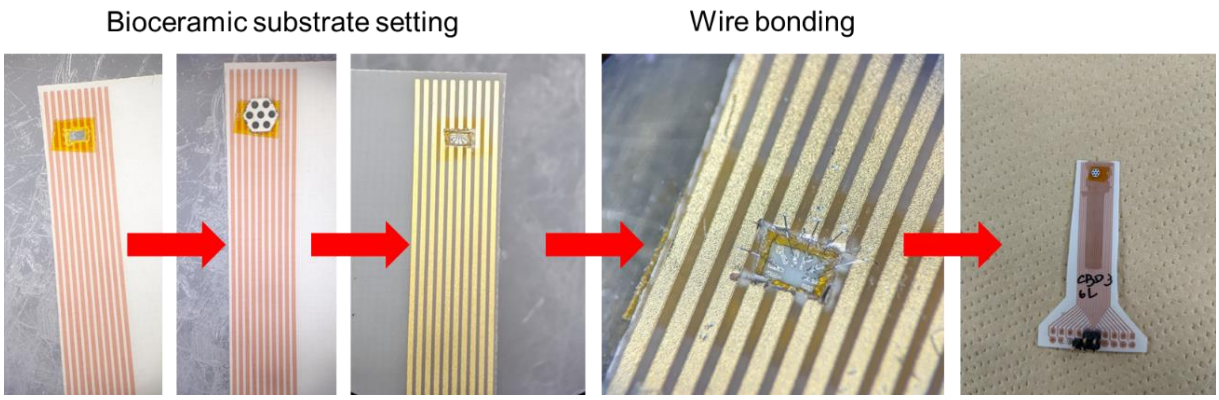


**Figure 4.3** The graphic flowchart for the wiring process

### 4.2.1 Cyclic voltammetry (CV)

Cyclic voltammetry (CV) was conducted using a potentiostat/galvanostat in a three-electrode setup. The working electrodes were CBD-derived and sputtered iridium oxide microelectrodes. A platinum electrode served as the counter electrode, and Ag|AgCl was used as the reference electrode. The CV measurement is to calculate the cathodic charge storage capacity (CSCc), which is determined by the integration of cathodic current in a potential range between -0.6 and 0.8 V (water window) at a scan rate of 50 mV $s^{-1}$, which is the same electrical evaluation in section 3.1.5.2. The setup for electrochemical measurements is shown in Figure 4.4.

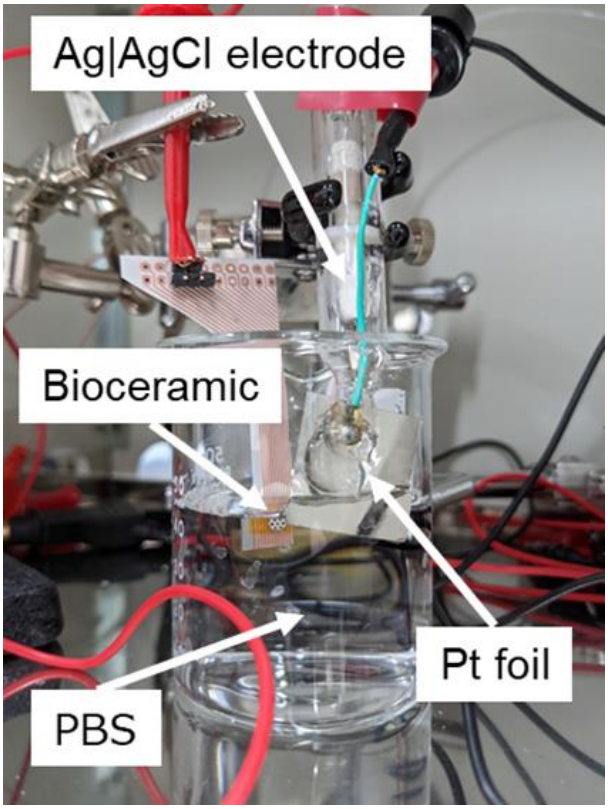


**Figure 4.4** The setup for electrochemical measurements

Figure 4.5 shows the CV profiles of the CBD-derived and sputtered iridium oxide microelectrodes. Cathodic-first neuron stimulation was used to determine the cathodic charge storage capacity (CSCc), to determine stimulation performance. The CSCc value is 62.1 ± 3.1 (n=4), 36.4 ± 1.6 (n=4) mC/cm$^2$, and 3.98 ± 0.26 (n = 5) mC/cm$^2$ for CBD-derived and sputtered iridium oxide and platinum microelectrodes. The cathodic charge storage for CBD-derived iridium oxide is 1.7 times higher than that of the sputter-derived iridium oxide.

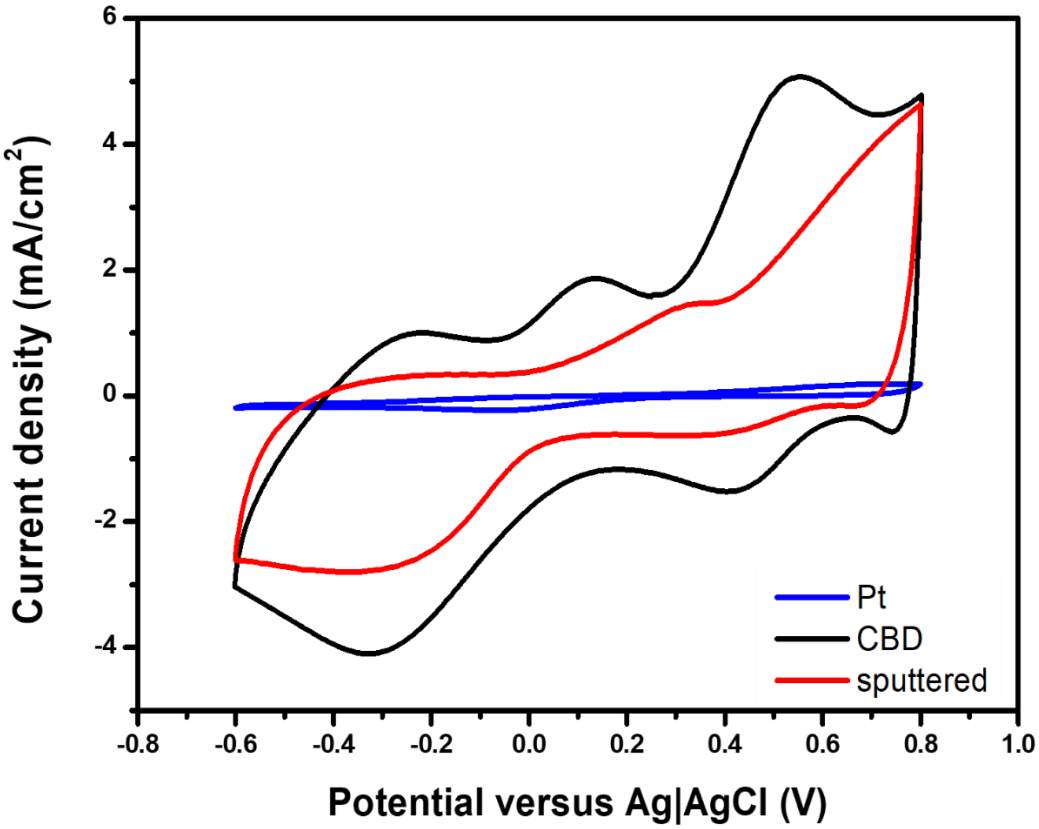


**Figure 4.5** The cyclic voltammetry profile for the CBD-derived and sputtered iridium oxide electrodes compared to the platinum electrode.

### 4.2.2 Voltage transient

The voltage transient is an electrochemical evaluation used to define the charge injection capacity (CIC) of the stimulating electrode. For the general voltage transient threshold (versus Ag|AgCl) in the iridium oxide electrode, the minimum cathodic voltage threshold is -0.6 V (Emc) and the maximum anodic voltage threshold is 0.8 V (Ema). The CIC analysis determines the maximum charge that can be injected across electrodes and electrolytes within -0.6 to 0.8 V versus Ag|AgCl. A charge balance is strictly required to avoid residual charge across the electrode interface, causing the neuron to be damaged during electrical stimulation. Thus, we

symmetrically applied cathodic-first biphasic current pulses in 0.5 ms duration per phase and 0.20 ms duration is used for resting inter-pulse.

Figure 4.6 displays a transient voltage profile in CBD-derived and sputtered iridium oxide electrodes. The maximum CIC value of CBD-derived iridium oxide electrode is 1.25 ± 0.09 $mC/cm^2$ (n=4) at 0.3 V bias potential, and for the sputtered iridium oxide electrode and platinum electrode are 0.68 ± 0.06 $mC/cm^2$ (n=4) and 0.07 ± 0.03 $mC/cm^2$ (n = 5). As a result, the CIC value for CBD-derived iridium oxide is 1.8 times higher than that of sputtered iridium oxide, and it is over 10 times higher than the CIC value of platinum.

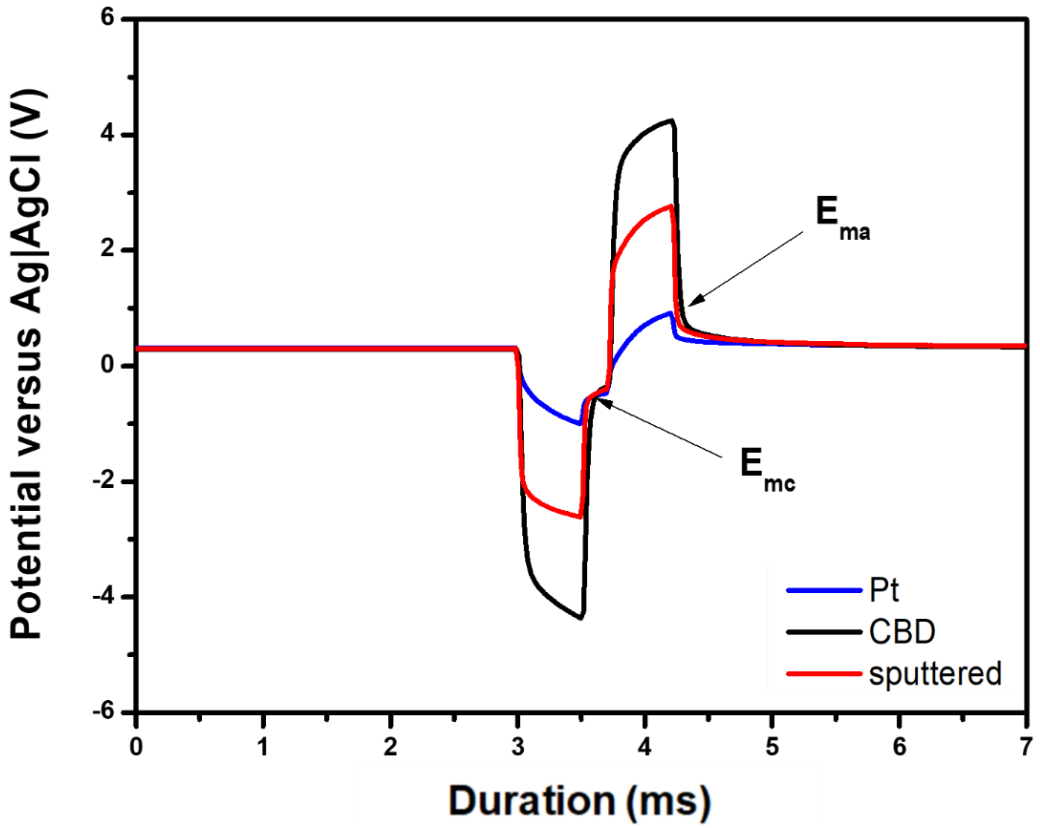


**Figure 4.6** The voltage transient profile for CBD-derived and sputtered iridium oxide electrode compared to the platinum electrode.

### 4.2.3 Electrochemical impedance spectroscopy (EIS)

Electrochemical impedance spectroscopy (EIS) was performed using a sinusoidal stimulation with an amplitude of 10 mV in the frequency range of 1–$10^5$ Hz at a constant 0.3 V bias. All electrochemical analyses were carried out in a commercial 0.01 M phosphate buffered saline at room temperature.

EIS was used to determine the impedance response across the electrode and electrolyte. The impedance response determines the efficiency of the neuron stimulation, and a lower impedance in the electrodes leads to a higher stimulation efficiency owing to the lower charge and energy loss released from the electrode interface. Apparently, the impedance response in platinum is much higher than iridium oxide (CBD or sputter derived) as shown in Figure 4.7. In Figure 4.7, the impedance response in the range of 10-1000 Hz shows that the impedance of the CBD-derived iridium oxide electrode is lower than that of the sputtered iridium oxide electrode. The impedance in 10 Hz is 2.43 ± 0.26 and 5.33 ± 0.59 kΩ for CBD-derive and sputtered iridium oxide, respectively.

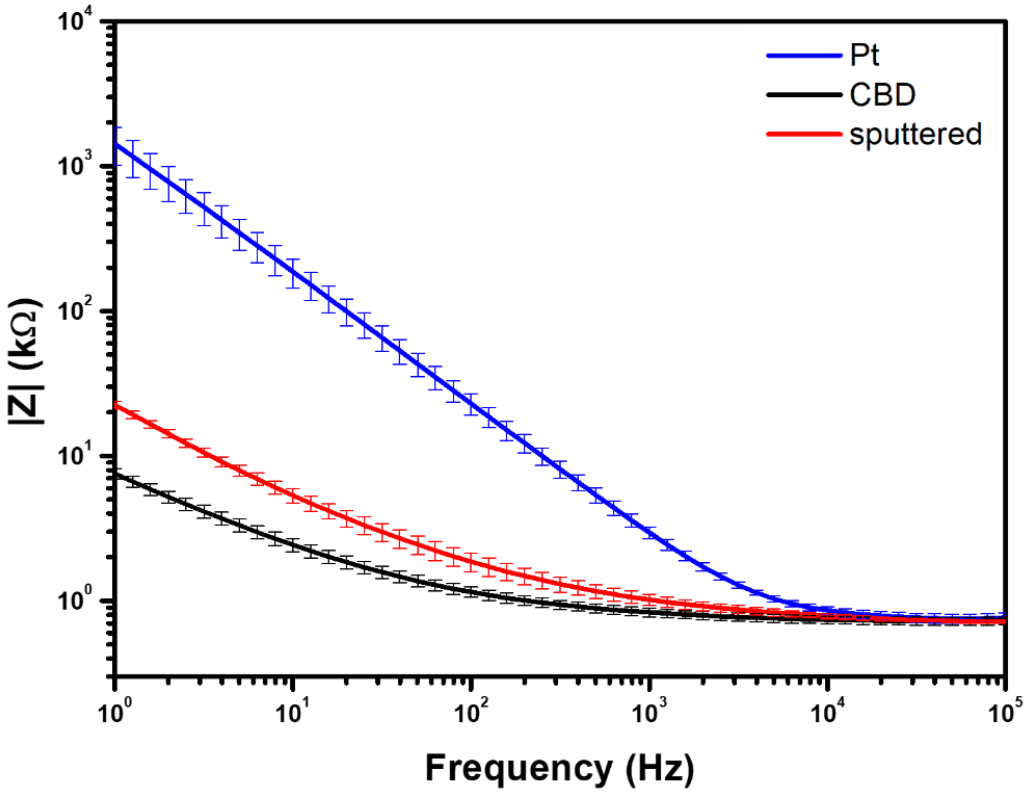


**Figure 4.7** The impedance responses for CBD-derived and sputtered iridium oxide electrodes compared to the platinum electrode.

## 4.3 Comparison of the CBD and sputtering processes of iridium oxide electrodes

In general, an iridium oxide film derived from sputtering deposition requires an adhesion layer such as titanium to improve the adhesion between common electrode-pad materials such as platinum or gold to obtain good adhesion, especially during voltage scanning or current input. Without the adhesion layer, the sputtered iridium oxide could undergo delamination due to the physical interlocking bond formation at the interface of the metal (platinum) and metal oxide (iridium oxide) in the sputtering process. It should be noted that the CBD-derived iridium oxide film was directly deposited on the platinum electrodes without using an adhesive layer. The CBD-derived iridium oxide electrode remained electrochemically stable after 1000 CV cycles

at an approximate value of 65.9 mC/cm$^2$ as shown in Figure 4.8. This is because of the formation of chemical bonds in the iridium oxide and platinum electrodes which provided strong adhesion. It is noted that the CSCc is getting larger after 1000 cycles of CV scans, and the redox faradaic pair peaks shift toward the lower voltage indicating the driving force for the faradaic reaction, such as $Ir^{3+}/Ir^{4+}$, in CBD-iridium oxide electrodes is smaller than 1$^{st}$ cycle CV scan. This might be owing to the microstructure of the film transforms into a more stable microstructure during the CV cycling.

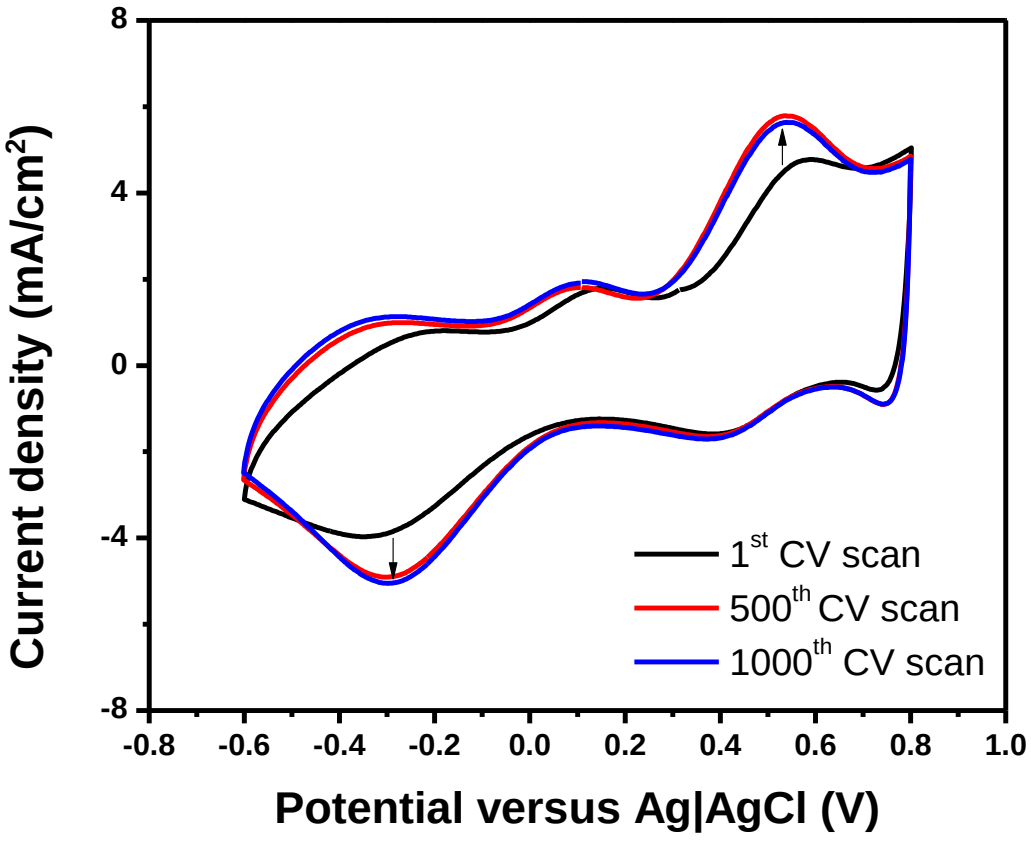


**Figure 4.8** The electrochemical durability for CBD-derived iridium oxide electrode

Generally, the CSCc value is positively proportional to the thickness of the electrodes due to the more iridium atom that could be induced the redox reaction in multiple iridium chemical

states such as $Ir^{3+}/Ir^{4+}$ to store more electrical charge.[18,20,21] The thickness of the CBD-derived iridium oxide is ~220 nm (62.1 ± 3.1 mC/cm$^2$) and that of the sputtered is ~630 nm (36.4 ± 1.6 mC/cm$^2$), indicating that the CBD-derived iridium oxide electrode provides a high-efficiency use of material. Normally, the thicker iridium oxide film could store more electrical charges, but it shows the opposite result, the thinner CBD-iridium oxide electrode stores, the more charge instead of the thicker sputtered iridium oxide film. This is due to the aqueous solution process in the fabrication of iridium oxide to provide more hydrate or hydroxide groups in the CBD-derived iridium oxide, which could supply more electroactive sites and compensation ions to induce the redox reaction in PBS as compared to the sputtered iridium oxide. This result is consistent with the XPS result, and the more nature hydroxide exists in the CBD-derived iridium oxide.

This maximum CIC value for CBD-derived electrodes in the area of 196,350 μm$^2$ is similar to other iridium oxide microelectrodes reported in the literature [22], and this value is satisfactory to achieve the neuron stimulation application reported in [22, 24-28]. In the CIC results comparison, the CIC value of the CBD-derived iridium oxide is 1.8 times higher than that of the sputtered, which is consistent with the CSCc results as well as the hypothesis associated with more electroactive sites and abundant hydroxide and hydrate groups in the CBD-derived iridium oxide electrode.

The frequency for the neuron stimulation application is approximately 10–1000 Hz; thus, the primary evaluation for impedance responses would be focused in the frequency range of 10–1000 Hz. In Fig. 13, the average impedance response in the range of 10–1000 Hz is 1.32 ± 0.12 and 2.31 ± 0.3 Ω for CBD-derived and sputtered, respectively, implying that the CBD-derived iridium oxide electrodes could provide more efficiency to deliver the charge from the electrode to the target neuron due to the lower impedance behavior.

As a result, the CBD-derived iridium oxide electrodes show a better electrochemical performance; however, the different thicknesses among the CBD (220 nm) and sputtered iridium oxide (630 nm) might also affect the charge storage capacity due to different intrinsic resistances. And also, the titanium layer was used in sputtered iridium oxide films as the adhesion layer resulting in an additional interfacial resistance between the Ti/Pt and Ti/iridium oxide. Unfortunately, the Ti layer is required to use for the sputtering iridium oxide process due to the poor adhesion in the film structure of the platinum and sputtered iridium oxide.

Hence, the chemical deposition of iridium oxide in this study provides a practical process to fabricate an iridium oxide thin film as a high-performance bio-interface, and the aqueous synthesis could potentially comply with the substrate in different shapes and morphologies.

## 4.4 Evaluation of the retinal device

### 4.4.1 Operation system and setup

The device was operated using a signal control box with a floating power supply system (FPSS). The counter electrode was connected to a voltage supply (VDD or VSS), and the switchable circuit was able to determine the cathodic or anodic current flowing to the stimulating electrode and the counter electrode obtained the biphasic current pulse stimulation, as shown in Fig. 4.9 (a). Details of the operation system were reported in our previous work [4].

The experimental setup of the device operation was conducted using a PC programmer, signal control box, received multiplexer, a platinum counter electrode, and oscilloscope, as shown in Fig. 4.9 (b). The PC programmer and signal control box defined the various current values that were fed to the selected electrodes. The device was connected to the received multiplexer to input signals from the signal control box. The device operation system was performed in the body median by immersing the device and platinum counter electrode into a phosphate buffered solution (PBS, Wako Pure Chemical Industries, Japan) at room temperature. A cathodic-first biphasic pulse was applied in the current range of 100-800 μA to evaluate the output current responses as designed. The final output current response was monitored using an oscilloscope. The detail operation of the program interface and a definition of the stimulation waveform is shown in Figure 4.10 and 4.11.

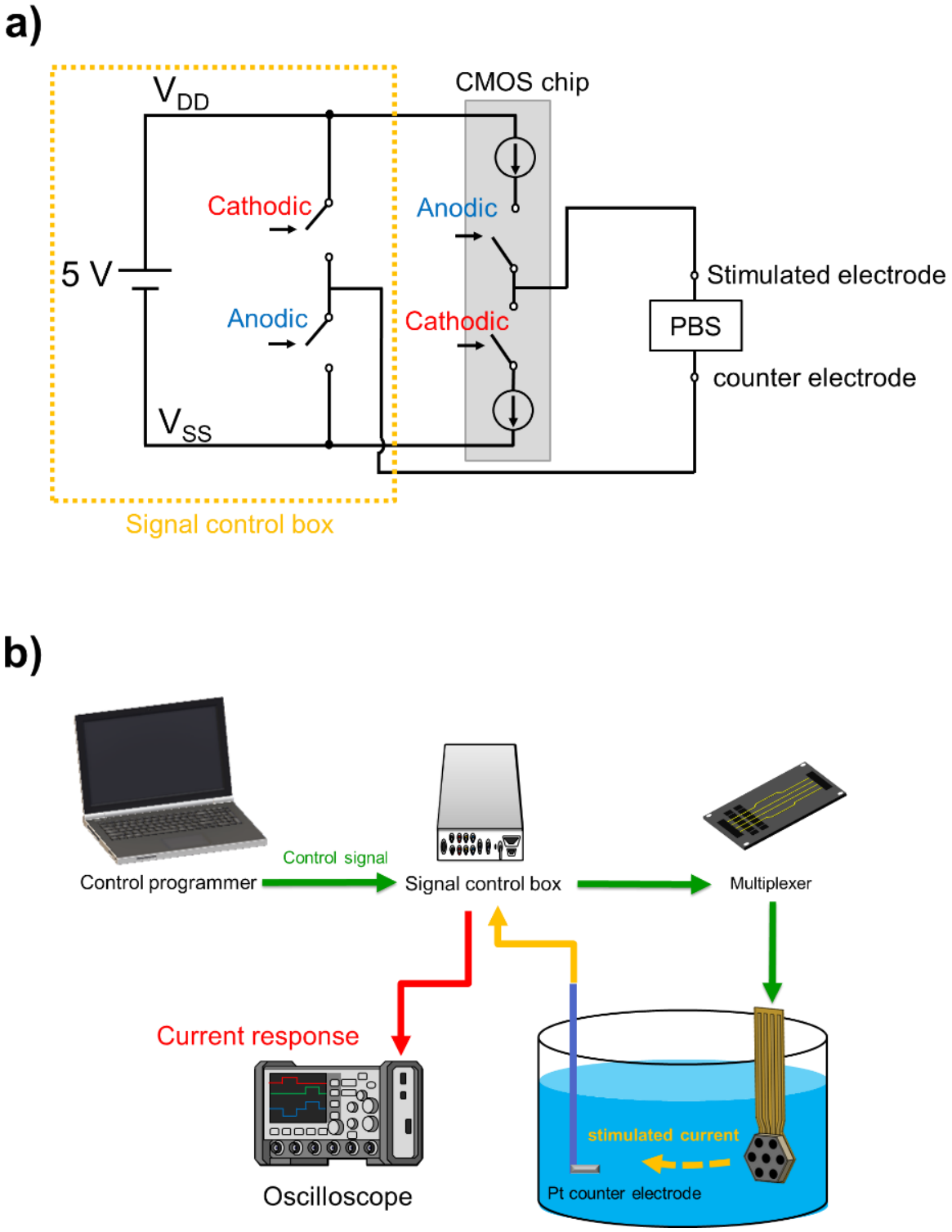


**Figure 4.9** The schematic of a) the operation system of the device, b) the experimental setup of the device operation

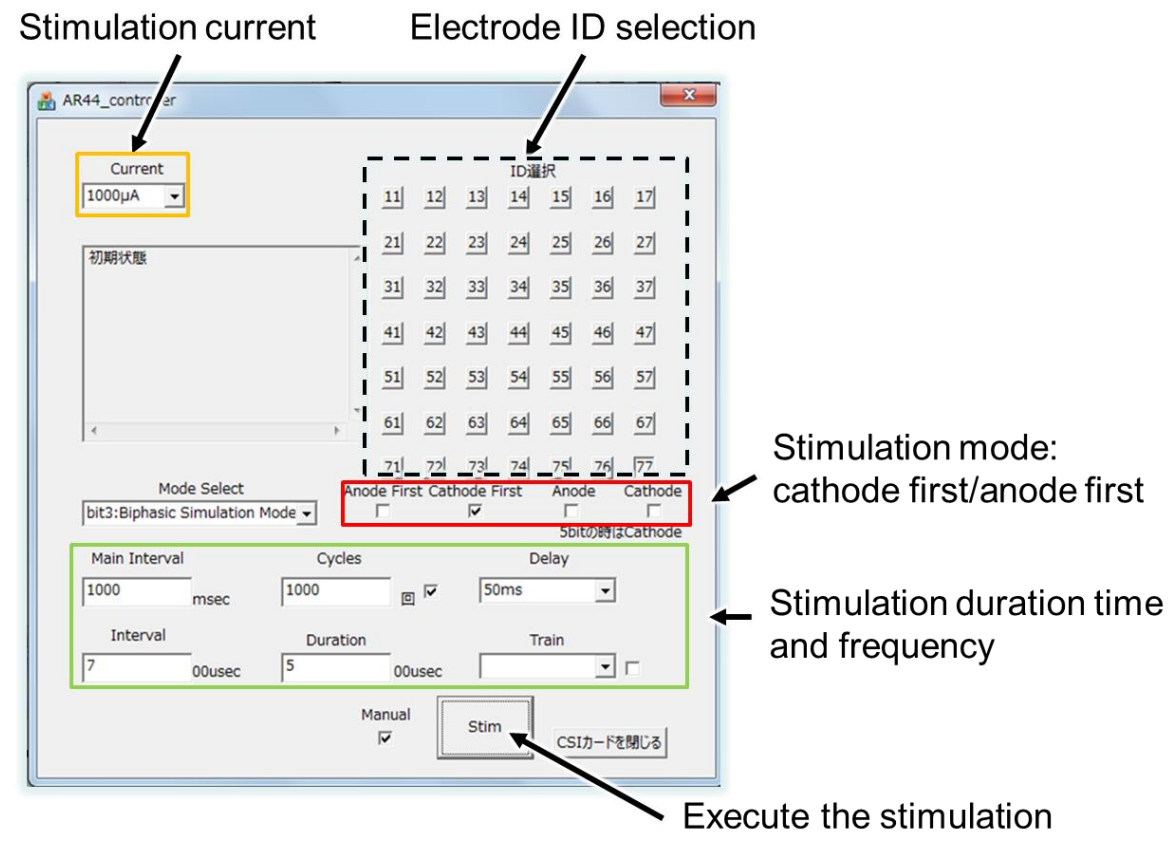


**Figure 4.10** The stimulation program interface

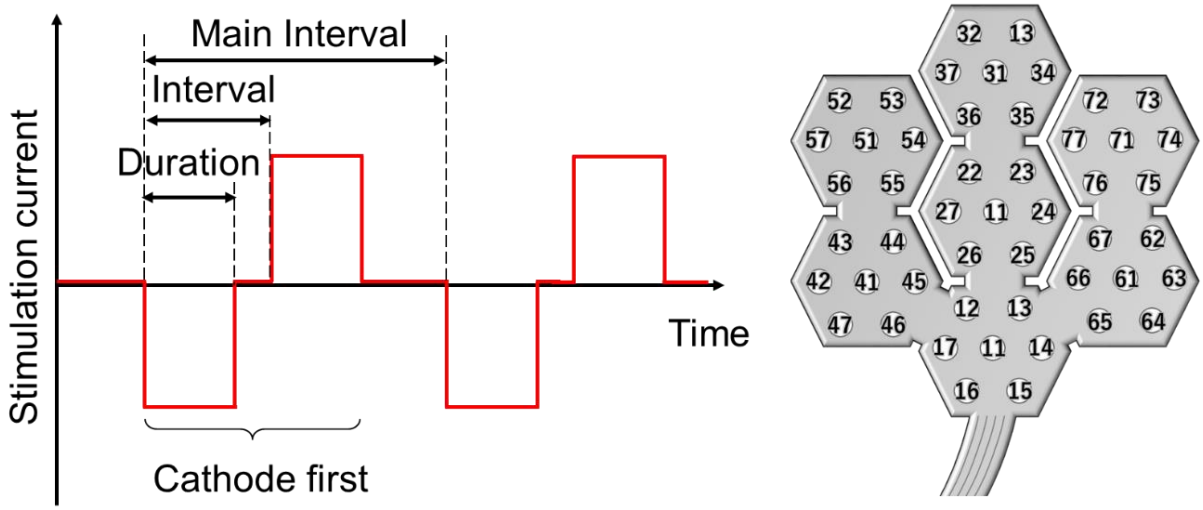


**Figure 4.11** The definition of the stimulation waveform and electrode IDs

## 4.5 *In vitro* experiment

To evaluate the device operation and performance, the device was operated at various input currents to verify that the stimulating waveform and value of the current are identical to the designed input currents. The current response results varied from the input 100-800 μA, as shown in Fig. 4.12. It showed that the device was able to generate the biphasic cathodic-first current pulse for 0.5 ms duration per phase, but the final stimulating current is less than the input current, with an approximate deviation of 15%. We compared the device performance with the previous work in developing the retinal device, as shown in Figure 4.13. As a result, the outputted current value in the device fabricated from the previous process is lower than that of the device fabricated from the new process. It could be explained in the better connection between the platinum interconnects and pads on the ceramic substrate, resulting in a less undesirable current consumption in the device fabricated from the new process.

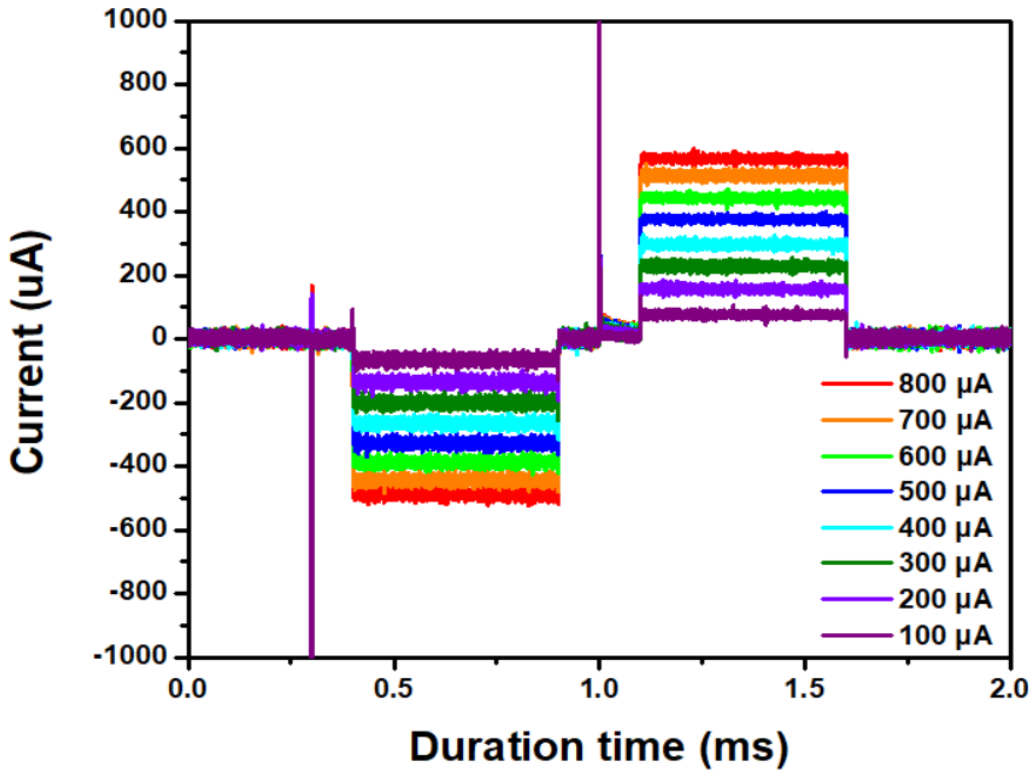


**Figure 4.12** The current response for the device performance in various input biphasic currents

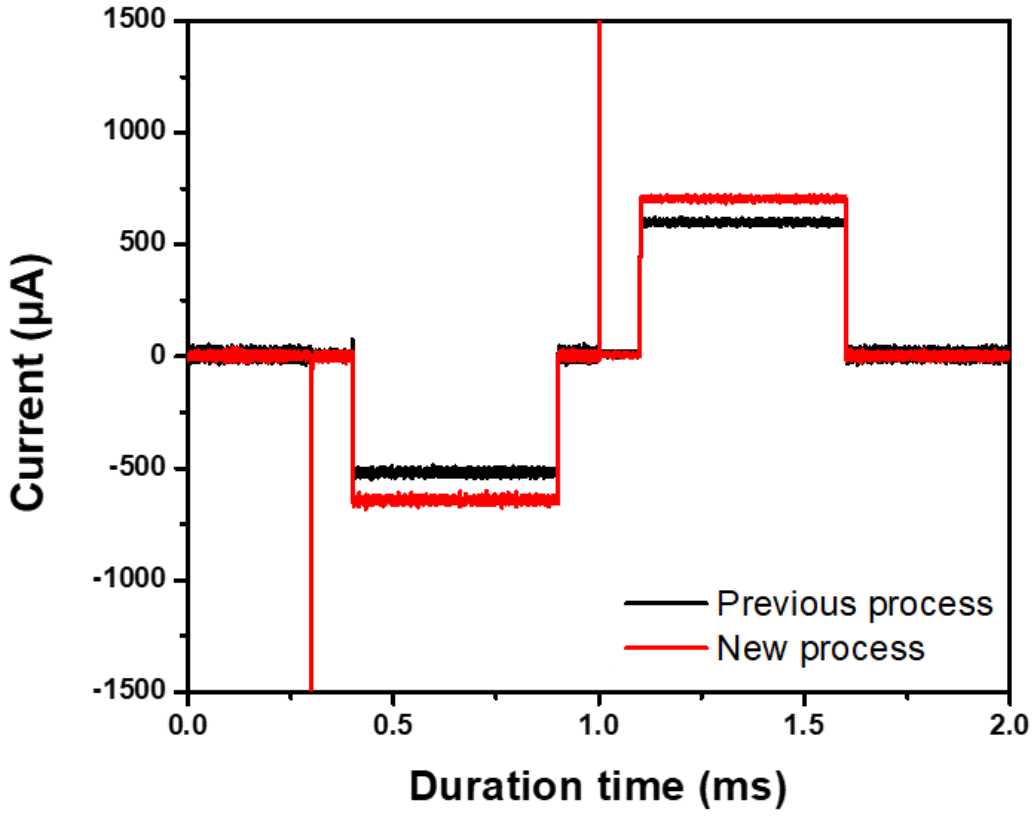


**Figure 4.13** The comparison of devices fabricated from the previous and new process in current response profile (800 µA)

The device successfully demonstrated a biphasic cathodic-first current pulse for a 0.5 ms duration per phase, as shown in Fig. 4.12. However, the stimulating current value of the retinal device did not operate in accordance with the designed current values. The current in the final stimulating current was approximately 15% less than the input current values. This deviation might be attributed to the undesirable current assumption in the device, such as platinum interconnects and CMOS chips. For instance, the resistance of platinum interconnects is measured to be 4.03 Ω, which is slightly higher than the ideal resistance value (1.06 Ω). This may be one of the factors that contribute to the unexpected current loss. Moreover, the device operation was conducted in PBS, resulting in an additional interface resistance between the electrode and electrolyte, leading to current deviation in the operation of the device. To sum up, the device could generate a sufficient amount of stimulating current for STS applications.

## 4.6 *In vivo* experiment

*In vivo* experiment was carried out after verifying the function of the retinal device in an *in vitro* environment (conducted in the PBS solution). In *in vivo* experiment, the target implantation position is a scleral pocket of a rabbit eyeball. Then, the implanted device performed the electrical stimulation in a current range of 800 to 1,200 μA.

### 4.6.1 *In vivo* experimental system

In animal experiment, a rabbit (11 weeks old, 2.4 kg) was used. The experiment was conducted under anesthesia and sedation. The rabbit was fasted from the day before the experiment to stabilize the deep level of anesthesia. After anesthetizing the rabbit and confirming the rabbit eyeball, the surgical knife was used to open the pocket space of the sclera. Next, the device was implanted into the pocket of the sclera and the device was programmed to operate the biphasic cathodic-first stimulation. Figure 4.14 shows the system of the *in vivo* experiment. The stimulation current waveform was measured by the oscilloscope connected with the device, the signal control box, the counter electrode inserted into the left foot. Figure 4.15 shows the implantation of the device in a cross-section view and an optical coherence tomography.

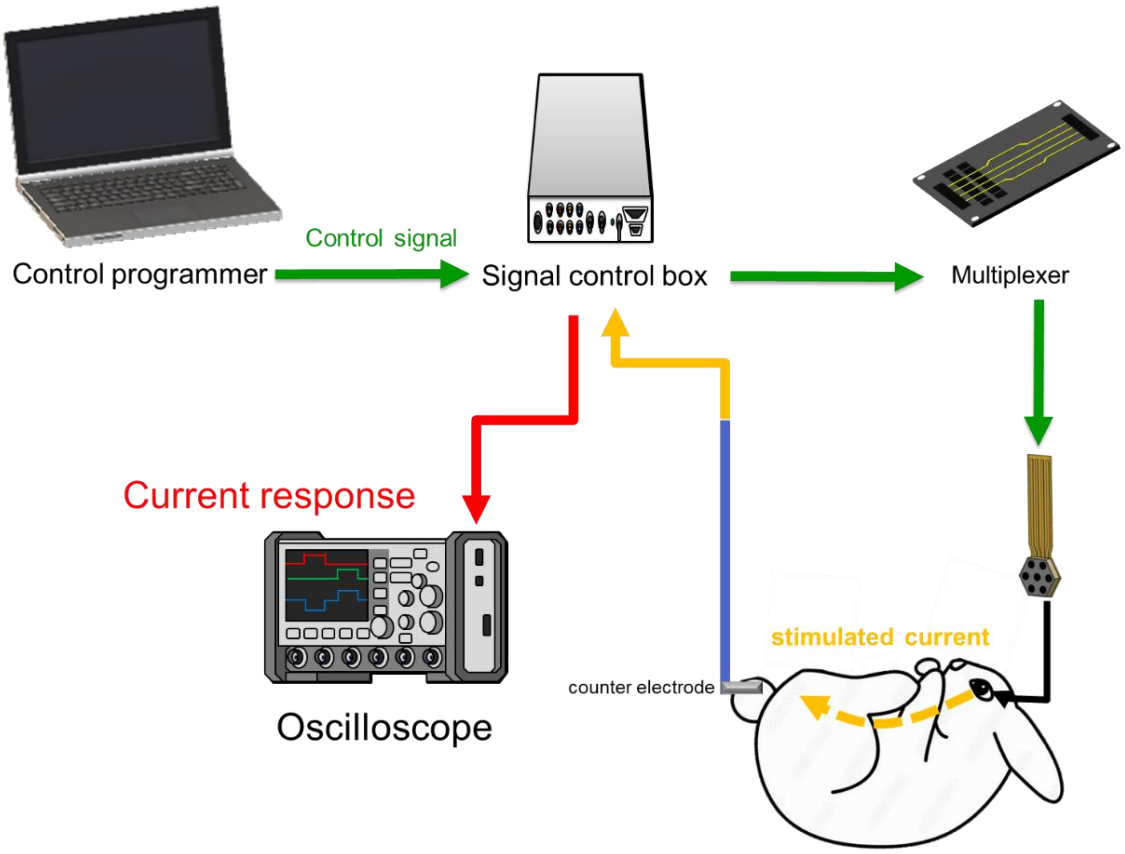


**Figure 4.14** The system for the *in vivo* experiment

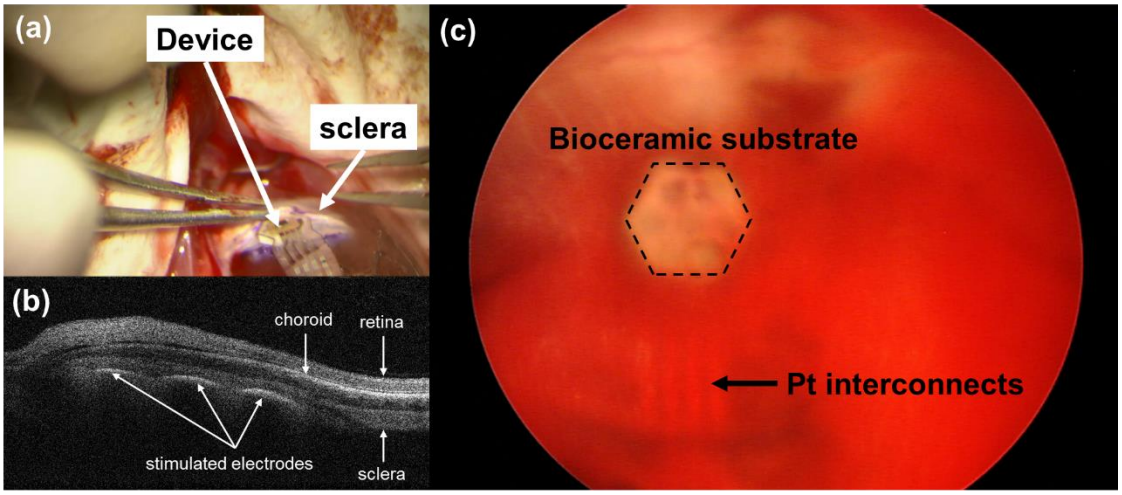


**Figure 4.15** The *in vivo* experiment photographs of (a) device implantation, (b) cross-sectional view of the rabbit eye, and (c) optical coherence tomography

### 4.6.2 *In vivo* measurement results

Figure 4.16 shows the stimulation waveform that applied to the sclera of the rabbit. From Fig. 4.16, the biphasic cathodic stimulation was successfully generated; however, the shapes of waveforms *in vitro* are significantly different. In addition, the cathodic current value becomes smaller as increasing the input current. Unfortunately, the device failed and could not be operating before we intended to verify the device response in the smaller value (less than 800 µA) of the stimulation current.

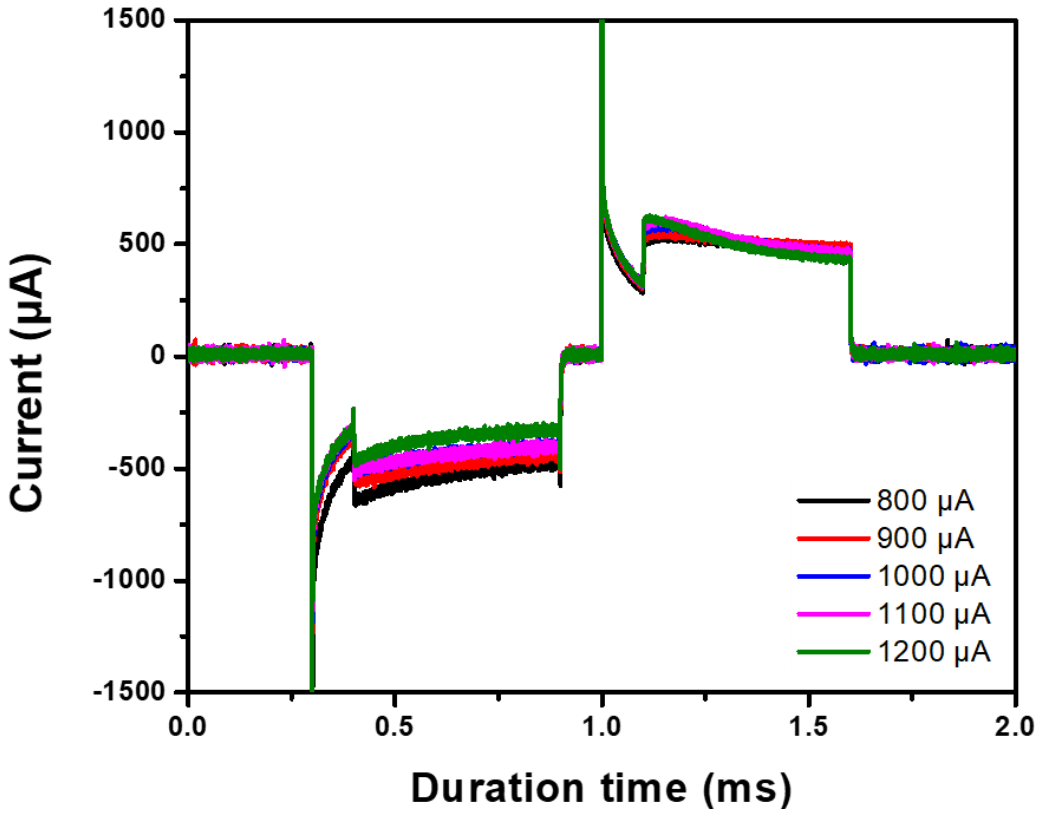


**Figure 4.16** The stimulation waveform in the *in vivo* experiment

### 4.6.3 Summary of the *in vivo* experiment

As a result, although the *in vivo* experiment was conducted using the developed device, the designed stimulation current waveform still could not be obtained. Moreover, the device broke down during the *in vivo* experiment. It might be because the parylene layer was damaged when the device was implanted into the pocket of the rabbit sclera, and the CMOS chip and the encapsulation for the Pt wiring were damaged and delaminated. Figure 4.17 shows the state of the device after implantation. Damage and exfoliation of parylene were confirmed on both of the two devices used in the *in vivo* experiment.

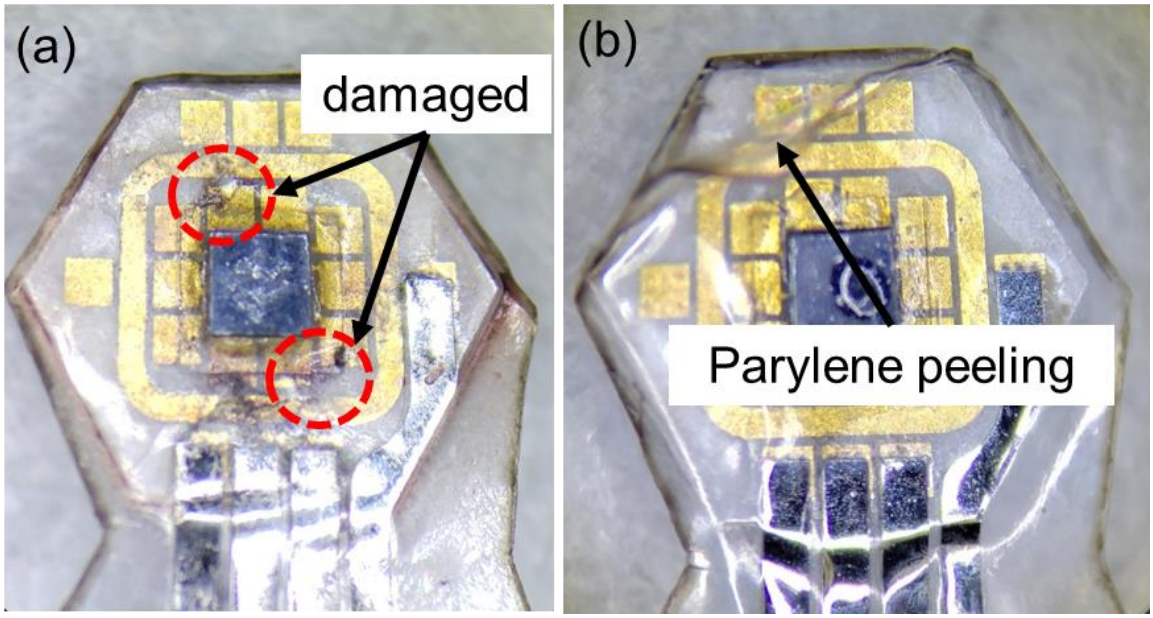


**Figure 4.17** Device after *in vivo* experiment

Fig. 4.18 shows the device is under *in vivo* experiment (conducted in the PBS) after *in vivo* experiment. From Fig. 4.18, bubbles occurred near the edge between the ceramic substrate and parylene. As a result, we concluded that not only the platinum interconnects but also the pads

on the ceramic substrate are contacted to the electrolyte or body fluid of the rabbit resulting from the parylene was peeled off. It results in the set current waveform that could not be fed as designed because the real signals could not be transmitted to the CMOS chip. Most of the current is consumed by water splitting reaction to generate the bubble in the PBS.

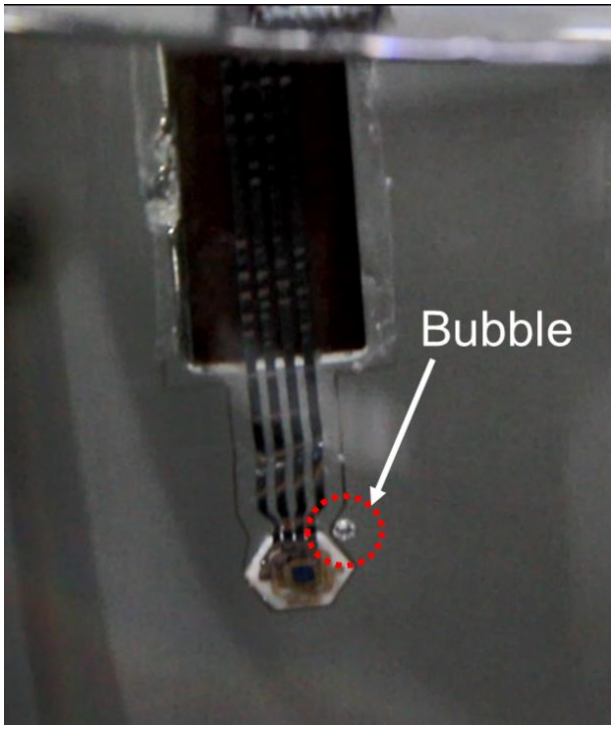


**Figure 4.18** The *in vitro* experiment after *in vivo* experiment

# 5. Conclusion

## 5.1 Summary

In this research, we have successfully developed a new manufacturing process for the honeycomb-type retinal device combined with the structure of the ceramic and flexible parylene aiming to obtain a high visual acuity, wide field of view, and promising long-term reliability, which are satisfied with the requirements for artificial visual devices. With the CMOS system, the stimulation action of seven electrodes could be controlled by only four platinum interconnects, which reduced the wiring number from 7 to 4, leading to a promising device structure for neuron stimulation.

The ceramic substrate, the most critical component to fabricate the device, is composed of the stimulation electrodes and the pads for CMOS chip installation. Until now, the process for fabricating the Pt interconnects on parylene and ceramic substrate has been considered the hardest issue. In the past, the process had been developed to form the platinum interconnects on the acrylic substrate. However, in the previous process, there is a problem that the efficiency of the ceramic mounting is lower while aligning the ceramic substrate to the acrylic substrate and platinum interconnects. Therefore, in this research, we have developed a new process to significantly increase the efficiency of the ceramic mounting and to successfully fabricate the device.

In the *in vitro* experiment, the new device was successfully operated and could generate the stimulation waveform as designed. Moreover, compared to the previous results, the new device performance is much closer to the desirable stimulation waveform and designed current values. To sum up, the new process is more efficient to fabricate the retinal device, and the new device can provide more accurate stimulation waveforms and current values.

Moreover, the CBD process was incorporated to fabricate an iridium oxide electrode that provides a facile synthesis of iridium oxide compared to the sputtering process. The electrochemical performance of the CBD-derived iridium oxide was greater than that of the sputtered iridium oxide. Therefore, the honeycomb-type retinal device adopted CBD-derived iridium oxide electrodes can provide a promising device structure for the retinal stimulation application.

## 5.2 Future outlook

In this research, we have developed a process for manufacturing the honeycomb type device with smart CMOS electrodes. The new process improves the device productivity and a reliable connection between platinum interconnects and pads of the ceramic substrate. However, there is remained some problem that needs to be developed and solved in device manufacturing.

First, the ceramic substrate size of 2.66 x 2.3 mm is only composed of 7 stimulation electrodes. From now device layout, it is difficult to manufacture a device that consisted of over

49 electrodes. In addition, the size of the ceramic substrate is too larger for the STS if we need high-resolution stimulation. Therefore, it is necessary to shrink the size of the ceramic substrate and the electrodes.

Second, the injected current used to stimulate the retinal neuron in our design remains the safety concern due to high current (around 1 mA) injections for the STS. The high current density might cause unexpected tissue damage during the stimulation. Therefore, it is necessary to verify the effect of high current stimulation from *in vivo* experiment. To overcome this issue, the size of the electrodes should be reduced so that the same charges can be injected into the electrodes with a lower current injection which might reduce the risk of high-current-induced damage to the retina.

Regarding the protection of the CMOS chip, especially during the *in vivo* experiment, it is necessary to consider proper protection methods for surgical implantations. Hermetic encapsulation with a glass lid could be considered as one of the protection methods [44]. A proper annealing process could also be considered to improve the adhesion among the platinum interconnects and parylene layer [45]. However, it is necessary to consider the possible effects of using ACP and $IrO_x$ as electrode materials. In addition, the layer number of the parylene could reduce as much as possible to obtain better encapsulation and device reliability.

# References

1. W. L. Wong, X. Su, X. Li, C. M. G. Cheung, R. Klein, C.-Y. Cheng and T. Y. Wong, The Lancet Global Health **2**, 106–116 (2014).

2. T. S. C. Friedman D S, McCarty C and De Jong P, Archives of Ophthalmology **122**, 564–572 (2004).

3. H. Tashiro, M. Kuwabara, Y. Nakano, Y. Terasawa, K. Osawa, Y. Yoshimura, H. Doi and J. Ohta, Sensors and Materials **30**, 251–268 (2018).

4. T. Noda, Y. Nakano, Y. Terasawa, M. Haruta, K. Sasagawa, T. Tokuda and J. Ohta, Japanese Journal of Applied Physics **57** (10), 1002B3 (2018).

5. Y. Terasawa, H. Tashiro, Y. Nakano and J. Ohta, Sensors and Materials **30,** 235–249 (2018).

6. P. D. Dalton, A. R. Harvey, M. Oudega and G. W. Plant, Tissue Engineering, 583–625 (2014).

7. R. A. Frederick, I. Y. Meliane, A. Joshi-Imre, P. R. Troyk and S. F. Cogan, Journal of Neural Engineering **17** (5), 056001 (2020).

8. E. Bloch, Y. Luo and L. da Cruz, Therapeutic Advances in Ophthalmology **11**, 1–16 (2019).

9. Y. H. Luo and L. da Cruz, Progress in Retinal and Eye Research **50**, 89–107 (2016).

10. T. L. Edwards, C. L. Cottriall, K. Xue, M. P. Simunovic, J. D. Ramsden, E. Zrenner and R. E. MacLaren, Ophthalmology **125** (3), 432–443 (2018).

11. E. Ho, X. Lei, T. Flores, H. Lorach, T. Huang, L. Galambos, T. Kamins, J. Harris, K. Mathieson and D. Palanker, Journal of Neural Engineering **16**, 066027 (2019).

12. T. Stieglitz, Journal of Neural Engineering **6** (6), 065005 (2009).

13. W. Tong, M. Stamp, N. V. Apollo, K. Ganesan, H. Meffin, S. Prawer, D. J. Garrett and M. R. Ibbotson, Journal of Neural Engineering **17** (1), 016018 (2019).

14. L. Bareket, A. Barriga-Rivera, M. P. Zapf, N. H. Lovell and G. J. Suaning, Journal of Neural Engineering **14** (4), 045002 (2017).

15. S. F. Cogan, Annual Review of Biomedical Engineering **10**, 275–309 (2008).

16. E. Slavcheva, R. Vitushinsky, W. Mokwa and U. Schnakenberg, Journal of The Electrochemical Society, 226–237 (2004).

17. J. Maeng, B. Chakraborty, N. Geramifard, T. Kang, R. T. Rihani, A. Joshi-Imre and S. F. Cogan, Journal of Biomedical Materials Research Part B: Applied Biomaterials **108** (3), 880–891 (2020).

18. S. F. Cogan, J. Ehrlich, T. D. Plante, A. Smirnov, D. B. Shire, M. Gingerich and J. F. Rizzo, Journal of Biomedical Materials Research Part B: Applied Biomaterials **89** (2), 353–361 (2009).

19. K. Stingl, K. U. Bartz-Schmidt, D. Besch, C. K. Chee, C. L. Cottriall, F. Gekeler, M. Groppe, T. L. Jackson, R. E. MacLaren, A. Koitschev, A. Kusnyerik, J. Neffendorf, J. Nemeth,

M. A. Naeem, T. Peters, J. D. Ramsden, H. Sachs, A. Simpson, M. S. Singh, B. Wilhelm, D. Wong and E. Zrenner, Vision Research **111**, 149–160 (2015).

20. J. D. Dorn, A. K. Ahuja, A. Caspi, L. da Cruz, G. Dagnelie, J. A. Sahel, R. J. Greenberg and M. J. McMahon, JAMA Ophthalmology **131** (2), 183–189 (2013).

21. P. H. Kuo, O. Y. Wong, C. K. Tzeng, P. W. Wu, C. C. Chiao, P. H. Chen, P. C. Chen, Y. C. Tsai, F. L. Chu, J. Ohta, T. Tokuda, T. Noda and C. Y. Wu, IEEE Transactions on Biomedical Engineering **67** (5), 1490–1504 (2020).

22. T. Fujikado, T. Morimoto, H. Kanda, S. Kusaka, K. Nakauchi, M. Ozawa, K. Matsushita, H. Sakaguchi, Y. Ikuno, M. Kamei and Y. Tano, Graefe's Archive for Clinical and Experimental Ophthalmology **245** (10), 1411–1419 (2007).

23. L. N. Ayton, P. J. Blamey, R. H. Guymer, C. D. Luu, D. A. Nayagam, N. C. Sinclair, M. N. Shivdasani, J. Yeoh, M. F. McCombe, R. J. Briggs, N. L. Opie, J. Villalobos, P. N. Dimitrov, M. Varsamidis, M. A. Petoe, C. D. McCarthy, J. G. Walker, N. Barnes, A. N. Burkitt, C. E. Williams, R. K. Shepherd and P. J. Allen, PLoS One **9** (12), e115239 (2014).

24. T. Fujikado, M. Kamei, H. Sakaguchi, H. Kanda, T. Morimoto, Y. Ikuno, K. Nishida, H. Kishima, T. Maruo, K. Konoma, M. Ozawa and K. Nishida, Investigative Ophthalmology & Visual Science **52** (7), 4726–4733 (2011).

25. L. Yue, P. Falabella, P. Christopher, V. Wuyyuru, J. Dorn, P. Schor, R. J. Greenberg, J. D. Weiland and M. S. Humayun, Ophthalmology **122** (12), 2545–2552 (2015).

26. A. K. Ahuja, J. Yeoh, J. D. Dorn, A. Caspi, V. Wuyyuru, M. J. McMahon, M. S. Humayun, R. J. Greenberg and L. Dacruz, Translational Vision Science & Technology **2** (4), 1 (2013).

27. H. Sailer, K. Shinoda, G. Blatsios, K. Kohler, L. Bondzio, E. Zrenner and F. Gekeler, Graefe's Archive for Clinical and Experimental Ophthalmology **245** (8), 1169–1178 (2007).

28. R. Daschner, U. Greppmaier, M. Kokelmann, S. Rudorf, R. Rudorf, S. Schleehauf and W. G. Wrobel, Biomedical Microdevices **19** (1), 7 (2017).

29. T. Fujikado, M. Kamei, H. Sakaguchi, H. Kanda, T. Endo, M. Hirota, T. Morimoto, K. Nishida, H. Kishima, Y. Terasawa, K. Oosawa, M. Ozawa and K. Nishida, Investigative Ophthalmology & Visual Science **57** (14), 6147–6157 (2016).

30. J. D. Weiland, D. J. Anderson and M. S. Humayun, IEEE Transactions on Biomedical Engineering **49**, 1574–1579 (2002).

31. I.-S. Lee, C.-N. Whang, J.-C. Park, D.-H. Lee and W.-S. Seo, Biomaterials **24** (13), 2225–2231 (2003).

32. I.-S. Lee, C.-N. Whang, Y.-H. Lee, G. Hwan Lee, B.-J. Park, J.-C. Park, W.-S. Seo and F.-Z. Cui, Thin Solid Films **475** (1-2), 332–336 (2005).

33. S. Thanawala, D. G. Georgiev, R. J. Baird and G. Auner, Thin Solid Films **515** (18), 7059–7065 (2007).

34. L. A. Geddes and R. Roeder, Annals of Biomedical Engineering **31**, 879–890 (2003).

35. L. Ouattara, S. Fierro, O. Frey, M. Koudelka and C. Comninellis, Journal of Applied

Electrochemistry **39**, 1361–1367 (2009).

36. R. K. Kawar, P. S. Chigare and P.S. Patil, Applied Surface Science **206**, 90-101 (2003).

37. J. Juodkazytė, B. Šebeka, I. Valsiunas and K. Juodkazis, Electroanalysis **17** (11), 947–952 (2005).

38. L. Badia-Bou, E. Mas-Marza, P. Rodenas, E. M. Barea, F. Fabregat-Santiago, S. Gimenez, E. Peris and J. Bisquert, The Journal of Physical Chemistry C **117** (8), 3826–3833 (2013).

39. M. Vukovic, Journal of applied electrochemistry **20**, 969–973 (1990).

40. S. J. Freakley, J. Ruiz-Esquius and D. J. Morgan, Surface and Interface Analysis **49** (8), 794–799 (2017).

41. T.-M. Chen, J.-Y. Hung, F.-M. Pan, L. Chang, S.-C. Wu and T.-C. Tien, Journal of Nanoscience and Nanotechnology **9** (5), 3264–3268 (2009).

42. A. J. Varkey and A. F. Fort, Thin Solid Films **235**, 47–50 (1993).

43. S. J. Freakley, J. Ruiz-Esquius and D. J. Morgan, The X-ray photoelectron spectra of Ir, $IrO_2$ and $IrCl_3$ revisited. *Surface and Interface Analysis* **49**, 794–799 (2017).

44. 遠藤 広基, “眼内埋植に向けたセラミック基板を用いた人工視覚用 CMOS スマート電極デバイス実装に関する研究,” 奈良先端科学技術大学院大学 修士学位論文 (2020).

45. R. P. Von Metzen and T. Stieglitz, Biomedical Microdevices **15**, 727–735 (2013).

# List of publications

**Journal articles:**

[1] **Kuang-Chih Tso**, Yuki Fukunari, Mizuki Hagita, Makito Haruta, Hironari Takehara, Hiroyuki Tashiro, Kiyotaka Sasagawa, Pu-Wei Wu, Jun Ohta, "Honeycomb-type Retinal Device using Chemically derived Iridium Oxide Biointerfaces", 2021, AIP Advances, vol. 11, 095305.

[2] **Kuang-Chih Tso**, Yi-Chieh Hsieh, Jyh-Fu Lee, Chih-Wen Pao, Po Chun Chen, Jun Ohta, Pu-Wei Wu, "Sequential oxidative-reductive formation of Na-doped iridium oxide with enhanced bio-stimulating performance", 2021, Chemical Communications. [submitted]

[3] **Kuang-Chih Tso**, Yi-Chieh Hsiehc, Tzu-Ying Chan, Jyh-Fu Lee, Jun Ohta, Pu-Wei Wu, "Recycling $IrO_2$ by a concentrated hydrochloric acid treatment", 2021, Results in Physics. [To be submitted]

[4] **Kuang-Chih Tso**, Tzu-Ying Chan, Yen-Chen Lin, Wei-Ju Chao, Shih-Cheng Chou, Shih-Chin Pan, Jyh-Fu Lee, Jun Ohta, Po-Chun Chen, Pu-Wei Wu, "Fabrication of iridium oxide thin film on polyimide as a flexible bio-electrode", 2021. [To be submitted]

[5] Tsung-Lin Hsieh, Pei-Sung Hung, Chuan-Jyun Wang, **Kuang-Chih Tso**, Han-Yi Wang, Yu-Che Lin, Chien-Tai Cheng, Ren-Jei Chung, Kung-Hwa Wei, Pu-Wei Wu*, Po-Chun Chen,

"Synthesis of $IrO_2$ Decorated Core-Shell PS@PPyNH$_2$ Microspheres for Bio-Stimulating Application", 2020, Nanotechnology, vol. 31, 375605.

[6] Tsai-Wei Chung, Ming-Ting Hsieh, **Kuang-Chih Tso**, Ya-Chun Chu, Shuo-Hsiu Kuo, Chien-Tai Cheng, Jiashing Yu, Ting-Shan Chan, Pu-Wei Wu*, Po-Chun Chen, "Synthesis and Characterization of Iridium Oxide Thin Film via a Pre-Coordination Step for Bio-Stimulating Electrode Application", 2020, Ceramics International, vol. 46, 18648-18655.

[7] Yi-Chieh Hsieh, Han-Yi Wang, **Kuang-Chih Tso**, Chung-Kai Chang, Chi-Shih Chen, Yu-Ting Cheng, Pu-Wei Wu, "Synthesis of Stable $IrO_2$ Nanoparticles in Neutral Aqueous Solution for Bio-Ink Applications", 2019, Ceramics International, vol. 45, 16645-16650.

[8] Han-Yi Wang, Yi-Chieh Hsieh, **Kuang-Chih Tso**, Chung-Kai Chang, Yu-Ting Cheng, Pu-Wei Wu, Jyh-Fu Lee, "Combination of Electrophoresis and Electro-Flocculation for the Formation of Adhering $IrO_2$ pH Sensing Films", 2019, Electrochimica Acta, vol. 312, 291-298.

**International conference:**

[1] **Kuang-Chih Tso**, Han-Yi Wang, Pu-Wei Wu, Po-Chun Chen, Jyh-Fu Lee, “Wet chemical synthesis of IrOx film for biostimulating interface”, 2017, MRS Spring Meeting & Exhibit, Phoenix, Arizona, U.S.

[2] **Kuang-Chih Tso**, Han-Yi Wang, Yi-Chieh Hsieh, Hung-Hsuan Li, Pu-Wei Wu, Po-Chun Chen, “Facile Chemical Synthesis of Iridium Oxide Films for Bioelectronic Implants Applications”, 2017, Symposium on Engineering, Medicine, and Biology Applications, Hsinchu, Taiwan.

[3] **Kuang-Chih Tso**, Yi-Chieh Hsieh, Han-Yi Wang, Pu-Wei Wu, Po-Chun Chen, Jyh-Fu Lee, “Chemically-derived Iridium Oxide Films as Bio-Stimulating Electrodes for Implantable Silicon-Based Devices”, 2017, MRS Fall Meeting & Exhibit, Boston, Massachusetts, U.S.

[4] **Kuang-Chih Tso**, Yi-Chieh Hsieh, Hang-Yi Wang, Pu-Wei Wu, Jyh-Fu Lee, Po-Chun Chen, Chi-Shih Chen, “Deposition of $IrO_2$ on Artificial Retina for Cell Growth”, 2018, MRS Spring Meeting Exhibit, Phoenix, Arizona, U.S.

**Domestic conferences:**

[1] **Kuang-Chih Tso**, Yuki Fukunari, Yasuo Terasawa, Takurou Kouno, Hironari Takehara, Makito Haruta, Hiroyuki Tashiro, Kiyotaka Sasagawa, Jun Ohta, "Development of Implantable

Retinal Device with CMOS Smart Electrodes in Honeycomb Matrix", 2020, 2020 年電子情報通信学会ソサイエティ大会.

[2] **Kuang-Chih Tso**, Hiroki Endo, HironariTakehara, Makito Haruta, Hiroyuki Tashiro, Kiyotaka Sasagawa, Jun Ohta, "A honeycomb-matrix retinal prosthesis with chemicalderived IrOx electrodes for retinal disease application", 2020, 第 67 回応用物理学会春季学術講演会.

[3] **Kuang-Chih Tso**, Yuki Fukunari, Mizuki Hagita, Hironari Takehara, Makito Haruta, Takurou Kouno, Yasuo Terasawa, Hiroyuki Tashiro, Kiyotaka Sasagawa, Pu-wei Wu, Jun Ohta, "A hexagon-assembly retinal prosthesis with chemical-derived IrOx bio-interfaces", 2021, 第 68 回応用物理学会春季学術講演会.